Langtaosha (LTS) Preprint doi: https://doi.org/10.65215/ydw1ks77 This version posted November 19, 2025. The copyright holder for this preprint (which was not certified by peer review) is the author/funder. All Rights Reserved. No reuse allowed without permission.

A Mechano-Feedback Loop Orchestrated by SUN1/2 Governs Cellular Mechanoadaptation via Lamina-Associated Domain Remodeling

Yafan Xie[1†], Zhaoyan Zuo[1†], Yanjing Zhao[2], Liping Guo[2], Wei Xu[3], Juhui Qiu[1,4,*], Guixue Wang[1,4,*], Qin Peng[2,*]

[1] Key Laboratory for Biorheological Science and Technology of Ministry of Education, State and Local Joint Engineering Laboratory for Vascular Implants, Bioengineering College, Chongqing University, Chongqing 400030, China.

[2] Institute of Systems and Physical Biology, Shenzhen Bay Laboratory, Shenzhen 518132, China.

[3] College of Life Sciences, University of Chinese Academy of Sciences, Beijing 101408, China.

[4] Institute of Panvascular Biology, JinFeng Laboratory, Chongqing, 401329, China

* Address correspondence to: pengqin@szbl.ac.cn (Q.P.); wanggx@cqu.edu.cn (G.W.); jhqiu@cqu.edu.cn (J.Q.)

†These authors contributed equally

Abstract

SUN1/2, core components of the linker of nucleoskeleton and cytoskeleton (LINC) complex, transmit extracellular mechanical forces to nuclear lamina and chromatin. However, their role in regulating peripheral chromatin in mechanosensing and mechanoadaptation remains unclear. Using CRISPR/Cas9-mediated knockout of *Sun1* or *Sun2* in myoblasts, we identified a SUN1/2-dependent mechano-feedback loop. SUN1/2 depletion downregulates genes for cell adhesion (e.g., integrin α4) and mechanotransduction (e.g., talin, RhoA). The primary mechanism involves redistribution of heterochromatin from nuclear periphery to the nucleoplasm and remodeling of lamina-associated domains (LADs), as an adaptive response to the loss of SUN proteins. Furthermore, lamin A/C acts as a key downstream effector, consistently modulating adhesion-related gene expression through the remodeling of LADs. Functionally, knockout of either *Sun1/2* or *Lmna* aggravates differentiation defects in C2C12 myoblasts and abolishes adaptive responses to mechanical cues. This study provides proof-of-concept that nuclear mechanotransduction proteins can modulate cellular mechanoadaptation via a mechano-feedback loop, which coordinates LADs reorganization with the expression of upstream mechanotransduction genes.

Langtaosha (LTS) Preprint doi: https://doi.org/10.65215/ydw1ks77 This version posted November 19, 2025. The copyright holder for this preprint (which was not certified by peer review) is the author/funder. All Rights Reserved. No reuse allowed without permission.

GRAPHICAL ABSTRACT

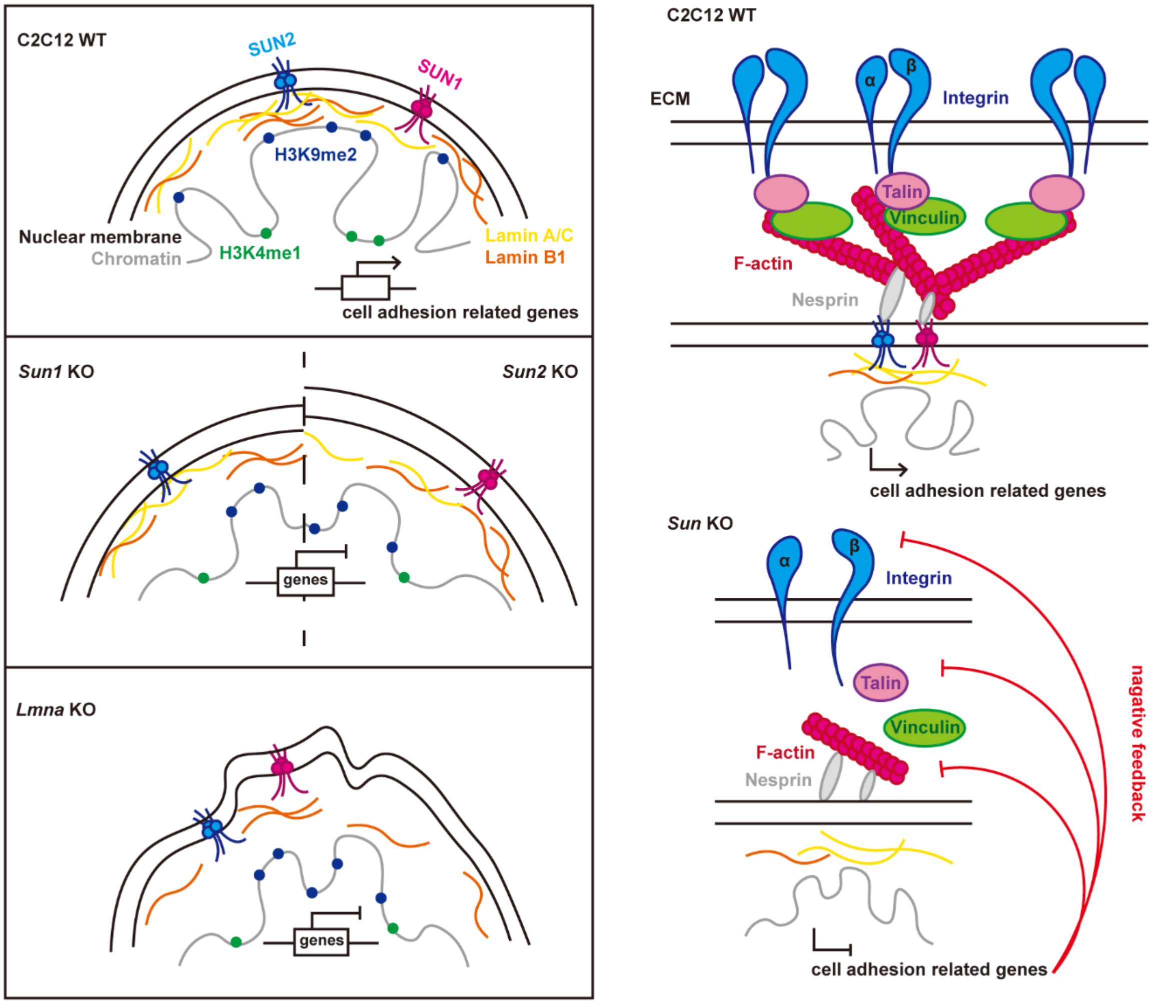

Proposed model for how nuclear core mechanical protein SUN1/2 and lamin A/C alter the cell mechanosensing and mechano-transduction via mechano-feedback, mediated LAD and chromatin re-organization. Knockout *Sun1*, *Sun2* or *Lmna* alters LAD formation and heterochromatin distribution, thereby inhibiting the gene expression of mechanosensing genes, such as integrin, and mechano-transduction genes, such as focal adhesion and small G protein (cdc42 and rac1), and then inhibit the cell adhesion and fate.

Highlights

- Knockout of *Sun1* or *Sun2* leads to marked downregulation of adhesion genes in stiffness cell.
- SUN1/2 is essential for maintaining nuclear-cytoskeletal integrity.
- SUN2 and lamin A are consistently regulating adhesion-related genes through LAD.
- Both SUN proteins and lamin A determine C2C12 differentiation.

Introduction

Cells are constantly exposed to dynamic mechanical cues in their microenvironment—such as shear stress, compression, extracellular matrix stiffness, and physical confinement—and they actively sense and adapt to these stimuli to maintain biochemical and biomechanical homeostasis[1-3]. This process, known as mechanoadaptation, is mediated by a coordinated mechanotransduction machinery: it begins with upstream force sensing through cell adhesion molecules like integrins, continues through midstream cytoskeletal remodeling and actomyosin-mediated generation, and culminates in downstream nuclear deformation and alterations in chromatin organization. These mechanical signals are ultimately translated into changes in gene expression and cell fate decisions[4-7]. Our prior research demonstrates that stress granules respond to shear stress and modulate integrin and inflammation genes expression[8, 9]. Recent advances have elucidated mechanoadaptive networks involving actin, microtubule, and calcium-mediated signaling that shape nuclear stability and transcriptional responses in mechanically challenged cells[10-12]. The nucleus functions not simply as a passive mechanosensing entity but as a central processing hub—integrating extracellular forces into chromatin reorganization, and transcriptional control[13-15]. This process, often termed mechanical feedback, involves mechanosensitive transcription factors that regulate gene expression to help cell adapt to their mechanical microenvironment[1, 16, 17]. However, how nuclear mechanics directly calibrates gene expression through mechanical feedback remains elusive.

A bidirectional mechanical bridge between extracellular forces and the nucleus is mediated by the linker of nucleoskeleton and cytoskeleton (LINC) complex[18]—comprising SUN (Sad1/UNC-84) -domain proteins in the inner nuclear membrane and KASH-domain proteins (e.g., Nesprins) in the outer membrane[19]. This complex mechanically couples the cytoskeleton to the nuclear lamina[20, 21], enabling force transmission and mechanotransduction. Importantly, genetic modulation SUN1/2 influences nuclear biophysical properties, including size, stiffness, and polarization, underscoring their functional importance in mechanosensitive cell behaviors[22]. For example, SUN2 suppression has been shown to soften the nucleus and delay cellular senescence induced by mechanical stress[22]. Additionally, SUN1 contributes to the regulation of cytoskeletal force generation and promotes focal adhesion maturation[23]. Nevertheless, how SUN1/2-driven mechanotransduction regulates gene expression for cellular adaptation remains unclear.

Gene expression under mechanical stimulation is highly dependent on chromatin architecture and epigenetic modifications[24-26]. A key feature of genome organization is the enrichment of transcriptionally repressive heterochromatin at the nuclear periphery, where it associates with nuclear lamina through regions known as Lamina-Associated Domains (LADs), and genes located in LADs are typically silenced, contributing to cell-type-specific transcriptional programs[27]. The nuclear scaffold protein lamin A/C plays a central role in modulating chromatin structure and stabilizing lamina-chromatin interactions[28, 29]. Besides, remodeling of cytoskeleton proteins such as F-actin, can also alter lamina-chromatin engagement and promote gene expression[30]. Given these findings, a critical question emerges: how do SUN1/2 contribute to genome organization—particularly in regulating the dynamics of LAD in response to mechanical cues?

Langtaosha (LTS) Preprint doi: https://doi.org/10.65215/ydw1ks77 This version posted November 19, 2025. The copyright holder for this preprint (which was not certified by peer review) is the author/funder. All Rights Reserved. No reuse allowed without permission.

In this study, we thus investigated the role of SUN1 and SUN2 in nuclear mechanotransduction and gene expression through an integrated multi-Omics approach. Our results demonstrate that SUN1/2 depletion induces nuclear enlargement and weakens cellular adhesion, which—through altered lamina-chromatin interactions—downregulates adhesion-related genes (such as integrin α4) and mechanotransduction genes. Consequently, reduced nuclear mechanosensitivity establishes a self-reinforcing feedback loop that further adaptively diminishes nuclear mechanical responsiveness. This loop unveils a fundamental mechanism by which the nucleus dynamically calibrates cellular mechanical responses through SUN-mediated transcriptional control of adhesion and mechanosensing programs.

Results

Knockout *Sun1* or *Sun2* decreases mechanotransduction related gene expression in myoblasts

The classical model of cellular mechanosensing and mechanotransduction, centered on the integrin-FAK-actin-LINC-lamina axis, represents a fundamental pathway through which cells perceive and adapt to external mechanical stress[18, 31, 32]. To elucidate the essential roles of SUN1 and SUN2 as mechanical conduits in force transmission to chromatin and their regulatory functions in mechanotransduction, we employed C2C12 myoblasts as a model system. Using CRISPR/Cas9-mediated gene editing, we successfully generated stable *Sun1* knockout (KO) and *Sun2* KO C2C12 cell lines (Fig.s S1A and S1B). RNA-seq analysis performed on wild-type (WT), *Sun1*KO, and *Sun2*KO cells revealed that depletion of either *Sun1* or *Sun2* led to substantial alterations in the transcriptome (Fig.s S2A, S2B, S2D and S2E). Specifically, gene ontology (GO) analysis indicated significant downregulation of terms associated with cell adhesion and muscle contraction (Fig. 1A). Notably, *Sun2* knockout resulted in downregulation of pathways related to actin filament organization, muscle contraction, and skeletal muscle contraction.

Focal adhesion (FA), the dynamic structure formed via specific molecular interactions between cells and the extracellular matrix, is the core structure for cell mechanical sensing and transduction[33, 34]. These connections are mainly mediated by integrins, which bridge extracellular matrix proteins and the intracellular cytoskeleton[35]. Among different types of cell lines, C2C12 cells, which has the highest cell stiffness, knockout of *Sun1* or *Sun2* led to marked downregulation of genes encoding integrins (e.g., *Itga4*, *Itga5*, *Itgb3*, *Itgb1*), adhesion complex components (e.g., *Vcl*, *Zyx*, *Tln2*, *Rhoa*), and cytoskeleton-regulated factors (e.g., *Capza1*, *Capza2*, *Ckap4*, *Rac1*, *Cdc42*) (Fig. 1B). Among these, integrin α4 exhibited the most reduction at the protein level and RNA transcription level (Fig.s 1C and S2C).

In contrast, in softer cell types, such as the circulating THP-1 cells[36], adipogenic cells[7], HUVEC[37] and CT26[38], depletion or reduction of SUN1 or SUN2 resulted in minimal changes in adhesion-related gene expression, and certain adhesive genes were even upregulated in soft adipocytes (Fig. 1B). These observations suggest that SUN1/2-mediated nuclear

Langtaosha (LTS) Preprint doi: https://doi.org/10.65215/ydw1ks77 This version posted November 19, 2025. The copyright holder for this preprint (which was not certified by peer review) is the author/funder. All Rights Reserved. No reuse allowed without permission.

mechanotransduction may attenuate the expression of upstream mechanosensing and mechanotransduction genes via a feedback mechanism, particularly in stiffer cellular contexts like C2C12 myoblasts, thereby recalibrating nuclear mechanical force homeostasis (Fig. 1D).

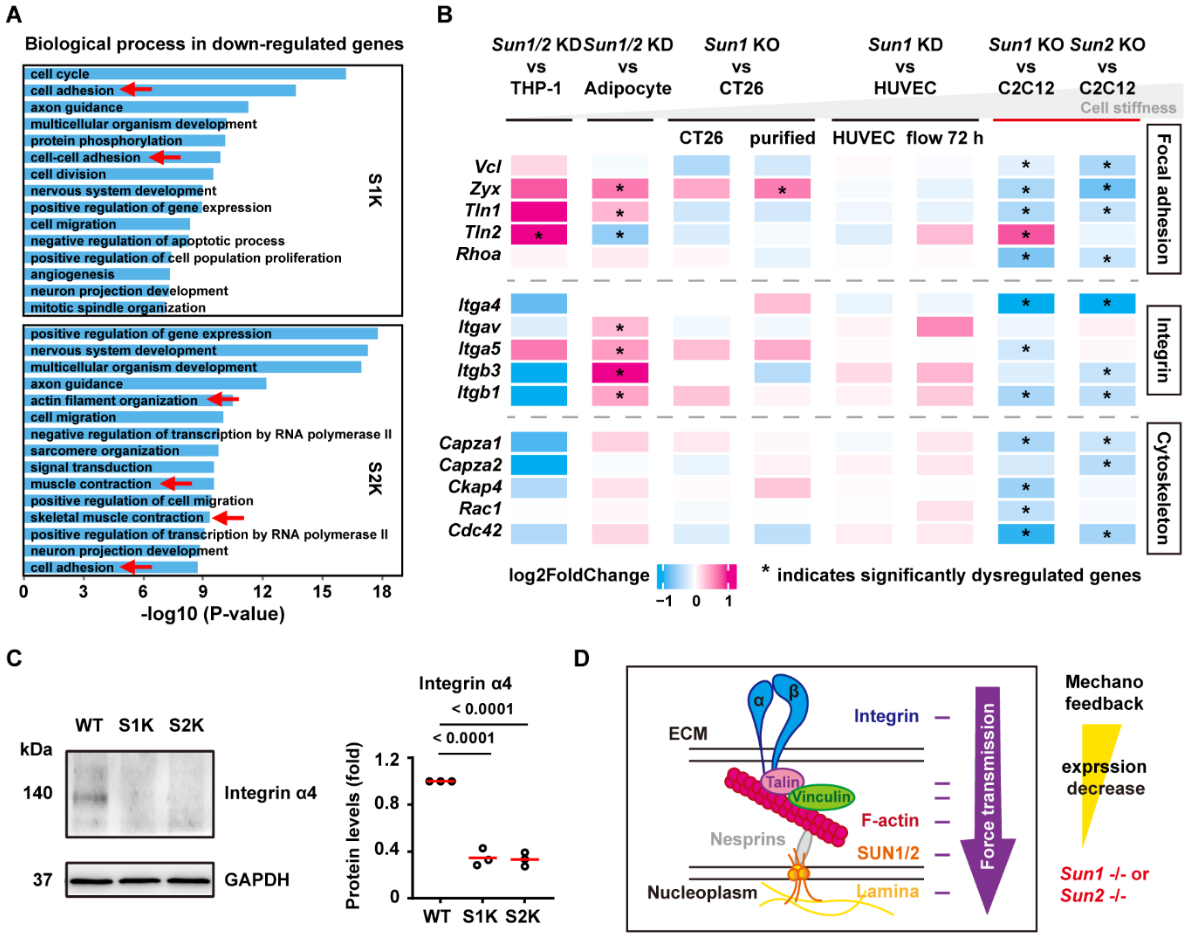

Fig. 1. Loss of SUN1 or SUN2 suppresses the upstream mechano-transduction genes expression.

(A) GO functional enrichment terms of significantly downregulated genes after knocking out *Sun1* or *Sun2*. Only the top 15 biological process terms are shown for each group. Red arrows indicate cell adhesion and cell force related terms.

(B) The heatmap shows the expression change levels of focal adhesion-related, integrin-related, and cytoskeleton-related genes. Asterisk indicates significantly dysregulated genes (FDR < 0.05 and Fold Change ⩾ 1.2). The cell stiffness from left to right is greater (gray; THP-1[39], CT26[40], HUVEC[41], Adipocyte < C2C12[42]).

(C) WB analysis of the representative down-regulated gene of integrin α4 protein levels in *Sun1* or *Sun2* knockout group (three biological replicates per group). Quantitative data to the right are

Langtaosha (LTS) Preprint doi: https://doi.org/10.65215/ydw1ks77 This version posted November 19, 2025. The copyright holder for this preprint (which was not certified by peer review) is the author/funder. All Rights Reserved. No reuse allowed without permission.

presented as the mean with SD. One-way ANOVA. WT: wild-type C2C12 cells; S1K: *Sun1*KO C2C12 cells; S2K: *Sun2*KO C2C12 cells.

(D) Schematic of the nuclear mechano-feedback that the upstream of mechanotransduction genes expression are inhibited by *Sun1* or *Sun2* knockout.

To further validate the mechanical feedback phenomenon, we performed immunofluorescence staining for F-actin and chromatin DNA to visualize the cytoskeleton and nuclei in C2C12 WT, *Sun1*KO, and *Sun2*KO cells. The distribution of perinuclear F-actin was examined across distinct cellular layers: the apical, middle, and basal regions. In WT cells, perinuclear F-actin exhibited a high-density, parallel arrangement. While *Sun1*KO cells displayed disorganized perinuclear F-actin in basal layer, which appeared misaligned relative to other layers. *Sun2* KO cells showed a more severe phenotype, with nearly absent perinuclear F-actin structures (Fig. 2A). To quantitatively assess these cytoskeletal alterations, we divided the basal view of the nucleus into nine equal segments and analyzed the perinuclear distribution of F-actin (Fig. 2B). Our results revealed a substantial reduction in basal perinuclear F-actin density in *Sun2*KO cells, accompanied by increased distance between F-actin and the nuclear envelope, which were corroborated through orthogonal views along the x-z and y-z axes (Fig. S3). We also observed that knockout of either *Sun1* or *Sun2* led to significant increases in nuclear volume and area (Fig.s 2C and 2D). And *Sun2*KO resulted in noticeable nucleus flattening (Fig. 2E).

We next investigated the impact of SUN1/2 depletion on FA by examining vinculin localization via immunofluorescence (Fig. 2F). Quantitative analysis revealed a decrease in the density of vinculin in both *Sun1*KO and *Sun2*KO cells compared to WT controls (Fig. 2G). Additionally, SUN1/2 deficiency increased the proportion of small vinculin-positive foci ($< 1\ \mu m^2$) (Fig. 2H). To probe the functional contractile response, we treated WT, *Sun1*KO, and *Sun2*KO cells with 1 nM Calyculin A—an inhibitor of protein phosphatases PP1 and PP2A that induces actomyosin contraction through myosin light chain (MLC) phosphorylation[43]. After 20 minutes of treatment, vinculin staining was used to evaluate FA density and size distribution (Fig.s 2F–H). While Calyculin A significantly reduced FA density and increased the abundance of small FAs ($< 1\ \mu m^2$) in WT cells, neither *Sun1*KO nor *Sun2*KO cells exhibited notable changes in FA morphology following treatment, indicating an impaired contractile response.

Collectively, these results demonstrate that SUN1/2 deficiency disrupts FA organization, cytoskeletal architecture, and nuclear morphology, underscoring its essential role in mechanotransduction and mechanical feedback regulation.

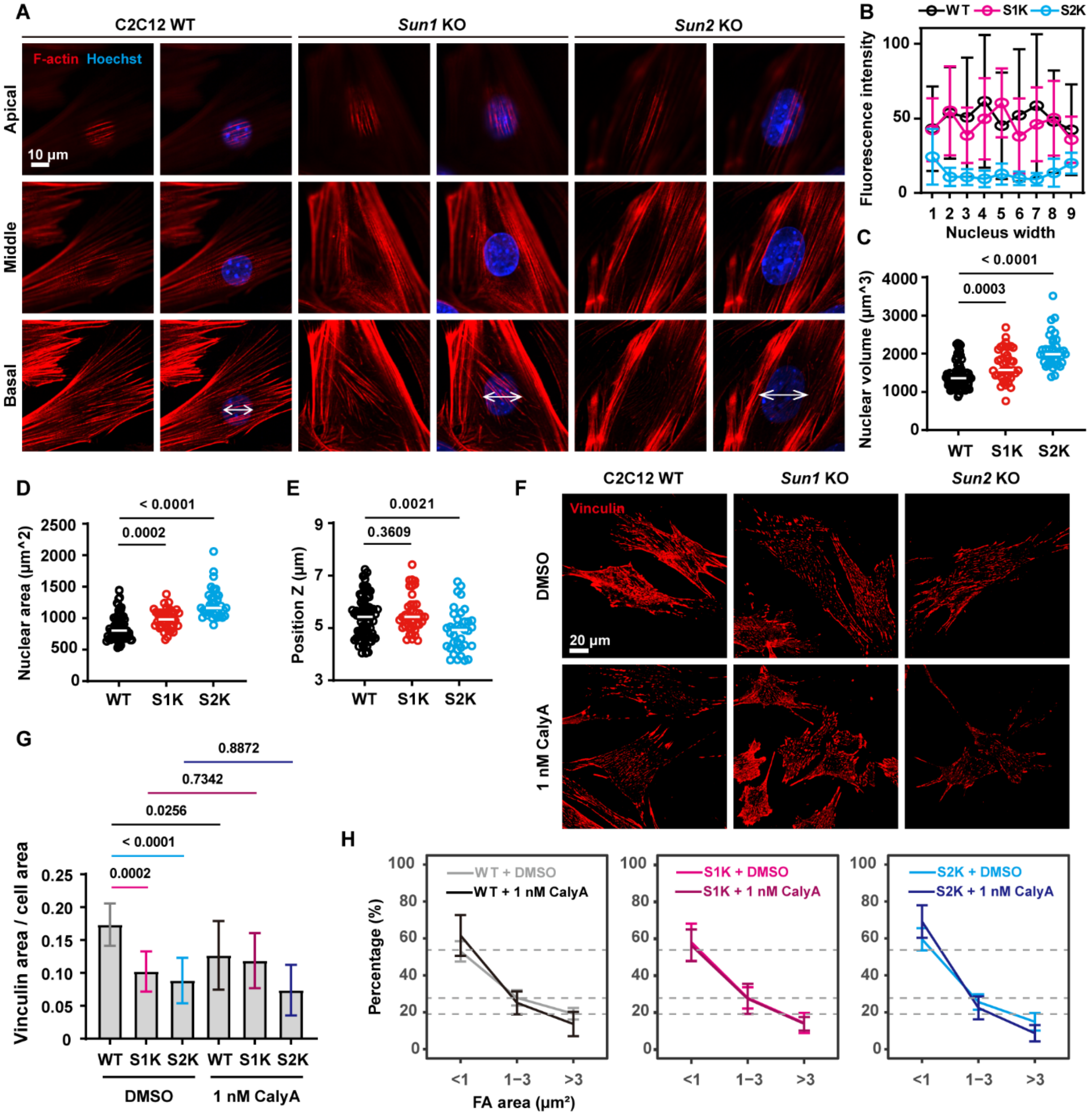

Fig. 2. SUN1 or SUN2 loss disrupts actin and inhibits FA.

(A) Immunofluorescence staining and imaging of nuclei and F-actin in C2C12 WT, *Sun1* KO, and *Sun2* KO cells (nuclei, n = 81, 44, 37 cells; F-actin, n = 7, 7, 7 cells). Images were taken from the apical, middle, and basal planes of the cells. Scale bar, 10 μm.

(B) Line graph showing the quantitative distribution of F-actin fluorescence intensity within the white line region in (A). The x-axis represents nine equal divisions of the measured region. Data are presented as the mean with SD.

Langtaosha (LTS) Preprint doi: https://doi.org/10.65215/ydw1ks77 This version posted November 19, 2025. The copyright holder for this preprint (which was not certified by peer review) is the author/funder. All Rights Reserved. No reuse allowed without permission.

(C-E) Quantitative analysis of nuclear volume (C), nuclear area (D) and nuclear height (E). Each dot represents an individual cell, and the white line segment indicates the mean value.

(F) Immunofluorescence staining and imaging of vinculin in C2C12 WT, *Sun1* KO, and *Sun2* KO cells (n = 9, 17, 10 cells) and cells treated with 1 nM Calyculin A for 20 minutes (n = 19, 18, 18 cells). Scale bar, 20 μm.

(G) Quantitative analysis of density of the FA, i.e., the total area of the vinculin divided by the cell area in each cell. Data are presented as the mean with SD. One-way ANOVA.

(H) Quantitative analysis of the proportion of FA with different volumes (< 1, 1-3, > 3 μm^2) in each cell. Data are presented as the mean with SD. Gray dash lines in three plots indicate the mean percentage of FA area in WT DMSO group.

S1K represents the *Sun1* KO cell, and S2K represents the *Sun2* KO cell in all the figures.

SUN1 and SUN2 regulates perinuclear chromatin dynamic distribution

Given the significant alterations in nuclear morphology and structure observed in *Sun1* KO and *Sun2* KO cells, we hypothesized that these changes might be associated with concomitant alterations in chromatin organization and histone modification. The trimethylation of histone H3 at lysine 9 (H3K9me3) serves as a well-established marker of heterochromatin, which ofter co-localizes with dense DAPI-stained regions, typically enriched at the nucleus periphery and around nucleoli[44]. To investigate this, we performed immunofluorescence staining for H3K9me3 and analyzed the resulting distribution patterns. The results showed that compared with C2C12 WT, the number of heterochromatic foci significantly increased in *Sun2* KO cells (Fig.s 3A-3C), while the size of heterochromatic foci was reduced in *Sun1* KO cells, with a predominant distribution in the 0.5-1 μm^3 or 0-0.25 μm^2 range (Fig.s 3D and 3E). These findings indicate that the loss of SUN1 or SUN2 disrupts the stability and nuclear organization of H3K9me3-marked heterochromatin, leading to its dissociation or fragmentation. Furthermore, we observed a notable redistribution of H3K9me2, another heterochromatin-associated mark, from the nuclear periphery toward the interior following *Sun1/2* depletion (Fig.s 3F-3H). This suggests a broader disruption of peripheral heterochromatin architecture. Consistent with these morphological changes, expression analysis of key enzymes regulating H3K9 methylation states showed a downregulation of genes encoding H3K9 methyltransferases and an upregulation of those involved in H3K9 demethylation (Fig.s S4A and S4B), further supporting the conclusion that SUN1/2 deficiency induces heterochromatic reorganization globally.

Langtaosha (LTS) Preprint doi: https://doi.org/10.65215/ydw1ks77 This version posted November 19, 2025. The copyright holder for this preprint (which was not certified by peer review) is the author/funder. All Rights Reserved. No reuse allowed without permission.

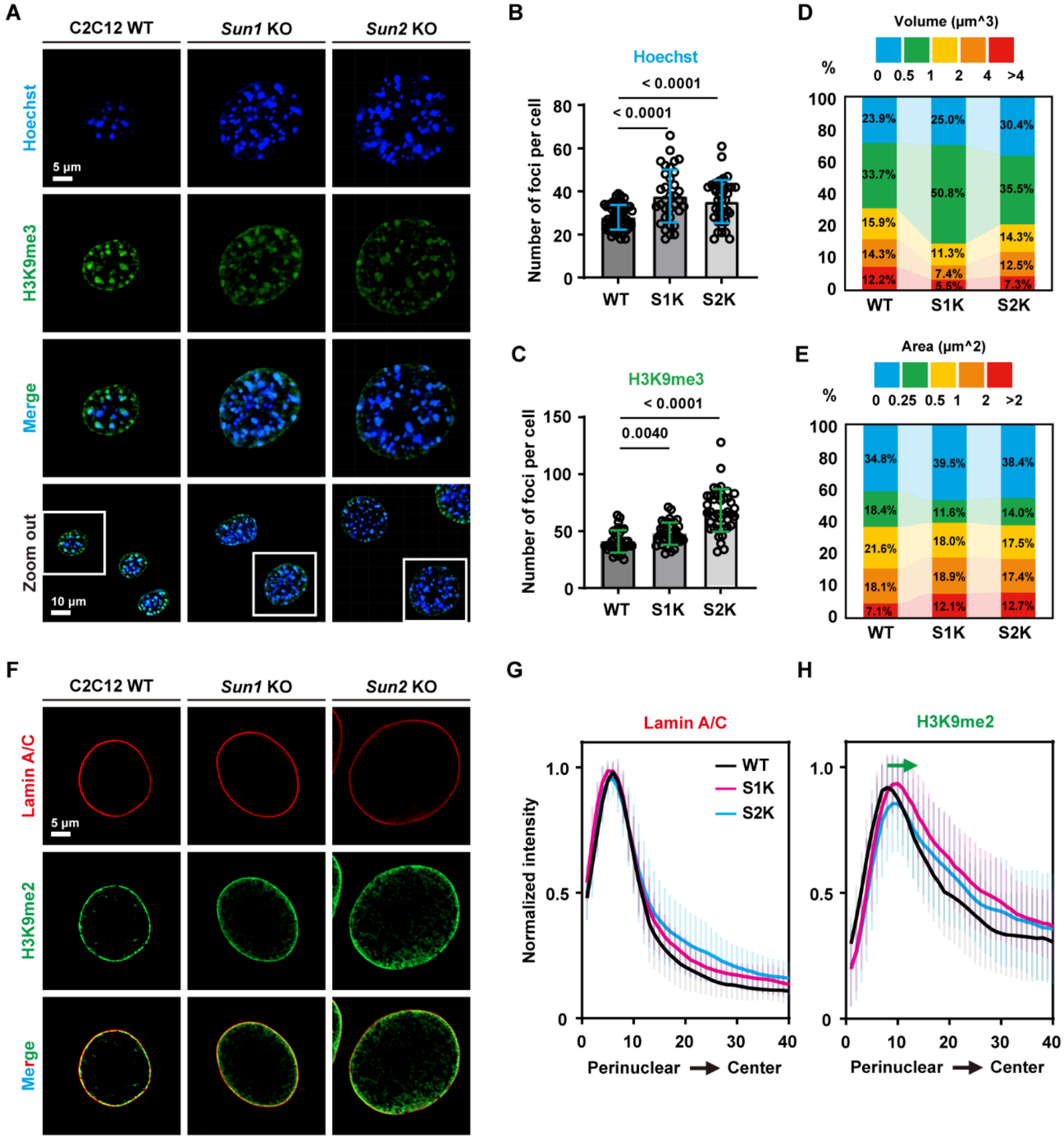

Fig. 3. *Sun1* or *Sun2* knockout regulates heterochromatic distribution.

(A) Immunofluorescence staining and imaging of the nuclei and H3K9me3 in C2C12 WT, *Sun1* KO, and *Sun2* KO cells (nuclei, n = 58, 34, 39 cells; H3K9me3, n = 34, 38, 41 cells). Scale bar, 5 μm, 10 μm.

(B and C) Quantitative analysis of the number of Hoechst-foci in 3D (B) and H3K9me3-foci in 2D (C) per cell. Each dot represents an individual cell. Data are presented as the mean with SD. One-way ANOVA.

(D and E) Quantitative analysis of the proportion of Hoechst-foci (D) and H3K9me3-foci (E) with

Langtaosha (LTS) Preprint doi: https://doi.org/10.65215/ydw1ks77 This version posted November 19, 2025. The copyright holder for this preprint (which was not certified by peer review) is the author/funder. All Rights Reserved. No reuse allowed without permission.

different volumes or areas in each cell.

(F) Immunofluorescence staining and imaging of the lamin A/C and H3K9me2 in C2C12 WT, *Sun1* KO, and *Sun2* KO cells (lamin A/C, n = 50, 40, 45 cells; H3K9me2, n = 50, 40, 45 cells). Scale bar, 5 µm.

(G and H) Line graph showing the distribution of lamin A/C (G) and H3K9me2 (H) fluorescence intensity across the nuclear periphery. Using the lamin A/C as the nuclear periphery boundary, the H3K9me2 displacement in *Sun1/2* KO cells was determined. The x-axis divides the segmented nuclear periphery to center (40 pixels). Data are presented as the mean with SD. The green arrow indicates the displacement phenomen.

S1K represents the *Sun1* KO cell, and S2K represents the *Sun2* KO cell in all the figures.

Heterochromatin always interacts with the nuclear lamina proteins, forming structures known as LADs. Genes embedded within LADs are typically transcriptionally repressed due to the peripheral localization and repressive chromatin environment [27], while other regions outside LADs, referred to as inter-LADs (i-LADs), are generally associated with a more open chromatin state and active transcription[45] (Fig. 4A). To elucidate the role of SUN1/2 in genome organization, we performed lamin B1 CUT&Tag sequencing in C2C12 WT, *Sun1*KO, and *Sun2*KO cells. LADs were identified in each group from the merged domains between two replicates and the intersection of LADs reveals 998 megabase (Mb) of constitutive LADs, and some variable LADs were unique to *Sun1*KO and *Sun2*KO cells (Fig. 4B). We then categorized the changes in LAD architecture following *Sun1/2* depletion into five distinct classes: Common LAD (cLAD), Lost LAD, Lost Edge, Gained LAD, and Gained Edge (Fig. 4C). The results showed that, *Sun1*KO led to an increase of 26 Mb in LAD and 41 Mb in LAD edge, while *Sun2*KO resulted in a gain of 32 Mb in LAD and 41 Mb in LAD edge. However, the loss of LAD and LAD edge was relatively less significant: a reduction of 16 Mb in LAD and 39 Mb in LAD edge was observed after *Sun1*KO, and a decrease of 14 Mb in LAD and 34 Mb in LAD edge after *Sun2*KO. Therefore, knocking out *Sun1* or *Sun2* resulted in a change in LAD composition and the acquisition of more LAD (Fig.s 4D-4F). Further analyze the length characteristics of the five types of LADs in each cell line. Compared with cLAD, the acquired or lost type of whole LAD or edge type LAD are smaller, indicating that they are more prone to unstable interactions with the nuclear lamina[46]. Notably, compared to *Sun1*KO, *Sun2* KO resulted in smaller gained LAD yet larger gained and lost edges (Fig.s 4G and 4H), highlighting isoform-specific regulatory roles in domain stability and boundary definition.

We next examined lamin B1 binding intensity across the different LAD categories. In *Sun1*KO cells, lost LADs exhibited a more convex binding profile, indicating pronounced disruption. Although cLAD is a positional invariant LAD, we observed a significant decrease in lamin B1 affinity for chromatin on cLAD, and lamin B1 enriched on the gained LAD or gained edge is less than that on the lost LAD or lost edge after the loss of SUN1, while loss of SUN2 is the opposite

Langtaosha (LTS) Preprint doi: https://doi.org/10.65215/ydw1ks77 This version posted November 19, 2025. The copyright holder for this preprint (which was not certified by peer review) is the author/funder. All Rights Reserved. No reuse allowed without permission.

(Fig.s 4I and 4J). The above results indicate that *Sun1*KO and *Sun2*KO have different characteristics of LAD composition changes. To understand the functional implications of these structural changes, we analyzed the genomic features of LADs. After knocking out *Sun1/2*, LADs showed a decreased association with promoter regions and were redistributed to more distal genomic areas (Fig. 4K). Specifically, we detected a loss of sequences within 10 kb of transcription start sites (TSS) and a concomitant gain of sequences over 100 kb away from TSSs (Fig. 4L). These findings demonstrate that SUN1 and SUN2 are critical regulators of LAD genomic positioning and connectivity, thereby influencing long-range chromatin organization and gene regulation.

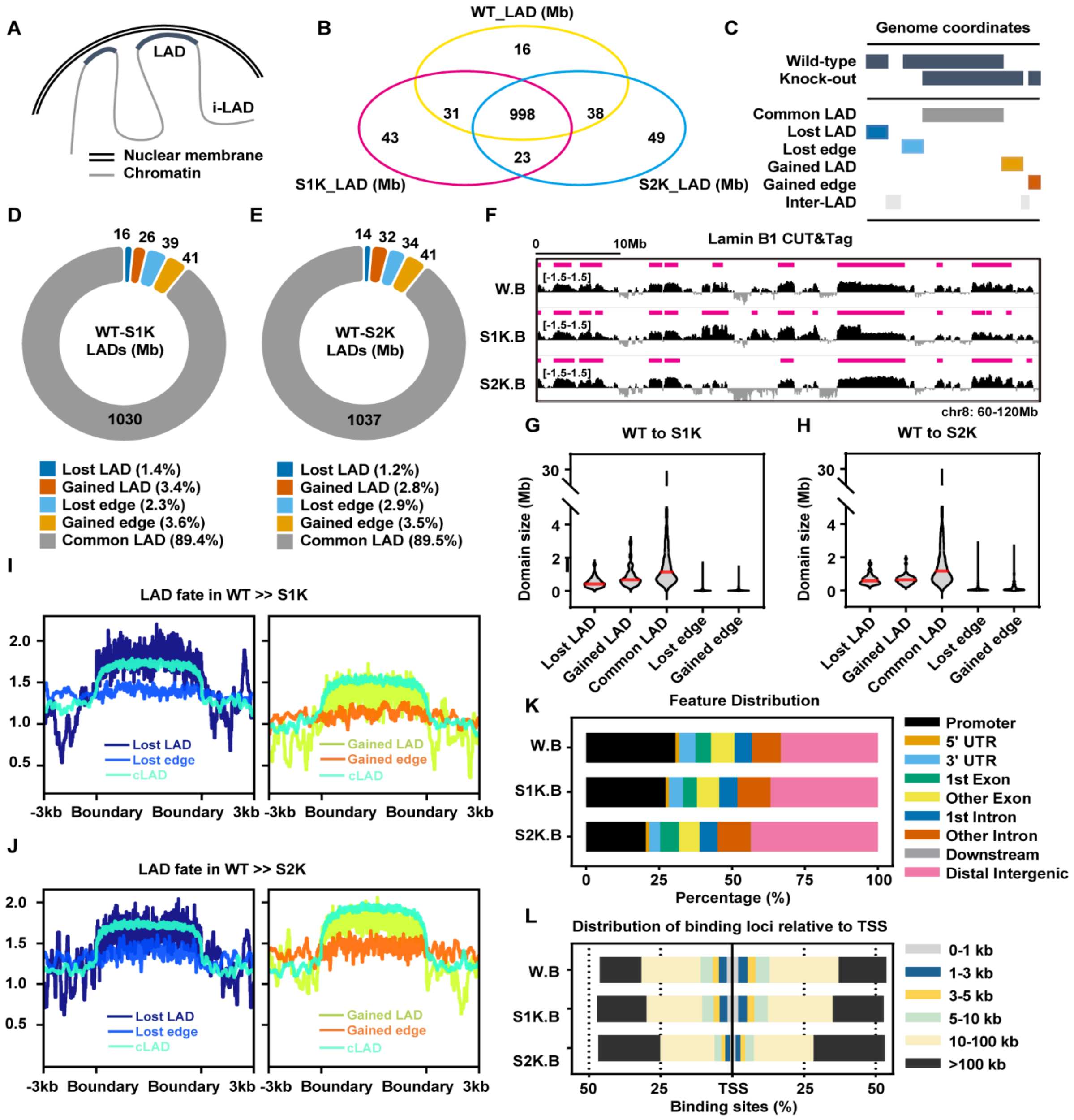

Fig. 4. LAD features after *Sun1* or *Sun2* knockout.

(A) Schematic representation of the distribution of LAD and i-LAD around the nuclear periphery.

(B) Venn diagram of genome coverage by LADs in C2C12 WT cells, *Sun1* KO cells, and *Sun2* KO cells. The unit is Mb.

(C) Definitions of five categories of LAD and i-LAD.

(D and E) Changes in the total length of five types of LADs, compared to C2C12 WT cells, in *Sun1* KO cells (WT-S1K) (D) and in *Sun2* KO cells (WT-S2K) (E). The unit is Mb, and the percentage in the legend represents the corresponding proportion of change.

(F) Gene views showing lamin B1 signals at chromosome 8 positions 60-120 Mb in C2C12 WT cells, *Sun1* KO cells, and *Sun2* KO cells. Red bars indicate identified LAD.

(G and H) Violin plots showing the domain size of five categories of LAD, comparing C2C12 WT cells to *Sun1* KO cells (WT to S1K) (G) and comparing C2C12 WT cells to *Sun2* KO cells (WT to S2K) (H). Red line segments represent the mean values.

(I and J) Distribution of lamin B1 signals within LAD and their boundaries (± 3 kb upstream/downstream) in (left) C2C12 WT cells and (right) *Sun1* KO cells (H) and in (left) C2C12 WT cells and (right) *Sun2* KO cells (I).

(K) Percentage distribution of gene features associated with lamin B1 binding sites in C2C12 WT cells, *Sun1* KO cells, and *Sun2* KO cells. Gene features include promoters, UTRs, exons, introns, and distal intergenic regions.

(L) Distribution of distances between lamin B1 binding sites and the nearest transcription start site. The genomic direction is 5’→3’.

W.B represents lamin B1 binding sites in C2C12 WT cell, S1K.B represents lamin B1 binding sites in *Sun1* KO cell, and S2K.B represents lamin B1 binding sites in *Sun2* KO cell in all the figures.

Lamin A/C acts as the key regulator in adhesion gene expression via LAD reorganization

Since SUN1/2 engages with lamin A through its N-terminal domain[19], we sought to determine whether lamin A deficiency impairs mechanotransduction and mechanical feedback regulation. To further elucidate the role of lamin A/C in LAD regulation, we performed transcriptomic analysis and observed significant downregulation of cell adhesion-related genes after knocking out *Lmna* (Fig.s 5A and S5)[47]. Given that heterochromatin histone modification H3K9me2 is associated with transcriptional repression[48], while active histone modification H3K4me1 marks active gene expression[49]. So, we hypothesized that lamin A/C may influence LAD-driven gene expression by modulating local chromatin states. Using immunofluorescence, we examined the distribution of H3K9me2 and H3K4me1 in C2C12 WT and *Lmna* KO cells. *Lmna* depletion led to a redistribution of H3K9me2 from nuclear periphery toward the interior (Fig. 5B), suggesting disrupted

Langtaosha (LTS) Preprint doi: https://doi.org/10.65215/ydw1ks77 This version posted November 19, 2025. The copyright holder for this preprint (which was not certified by peer review) is the author/funder. All Rights Reserved. No reuse allowed without permission.

heterochromatin anchoring. In contrast, the average fluorescence intensity of H3K4me1 remained unchanged. These epigenetic alterations were accompanied by severe nuclear deformation and loss of perinuclear lamin B1 staining after knocking out *Lmna* (S6A and S6B), indicating broad compromise of nuclear envelope integrity and chromatin organization in the absence of lamin A/C.

To further investigate the hierarchical regulation of the SUN1/2-lamin A/C-LAD axis, we performed lamin B1 CUT&Tag sequencing in C2C12 WT and *Lmna*KO cells. The results revealed a substantial reorganization of LAD architecture: *Lmna*KO led to a loss of 64 Mb in LAD and 52 Mb in LAD edge regions, while also triggering a gain of 25 Mb in LAD and 47 Mb in LAD edge (Fig. 5C). Consistent with this structural shift, lamin B1 enrichment across chromatin was dramatically reduced in *Lmna*KO cells compared to WT controls (Fig. 5D), indicating that lamin A/C deficiency disrupts LAD integrity and promotes LAD loss.

We further analyzed the epigenetic and genomic features of LADs. In *Lmna*KO cells, 525 loci with significantly increased lamin B1 affinity were unrelated to genes, while 1104 and 925 loci were linked to one or multiple genes, respectively, mainly distributed > 50 kb from TSS (Fig. S7A and S7B). Conversely, 8413 loci with reduced lamin B1 affinity were gene-associated primarily situated within 5 kb of TSS (Fig.s S7C and S7D). Although genes within LADs consistently exhibited low expression levels in both WT and *Lmna*KO cells (Fig. S7E), consistent with the repressive nature of LADs reported by previous studies[29], the overall correlation between LAD positioning and differential gene expression was negative but not strictly deterministic (Fig. S7F and Fig. S7G). These findings indicate that *Lmna* depletion shifts LADs from promoter-proximal to distal genomic regions and diminishes gene-associated sequences near TSS, paralleling phenotypes observed in *Sun1/2*KO models. However, LAD reorganization did not always correlate with gene expression changes, suggesting additional epigenetic mechanisms influence transcriptional output.

To assess the role of histone modifications, we performed CUT&Tag for H3K9me2 (defining heterochromatic KDD domains) and H3K4me1 (marking active KMD domains) in WT and *Lmna*KO cells. *Lmna*KO resulted in a loss of KDD (135 Mb) (Fig. 5E), yet increased global H3K9me2 levels and slightly elevated its promoter binding (Fig.s 5F and S8). Conversely, KMD sites increased (6677 loci), but H3K4me1 modification at promoters decreased (Fig.s S9A–S9C). PCA analysis revealed that upon *Lmna*KO, repressive KDD domains diverged from LADs, while active KMD domains converged toward them (Fig. S10). This reconfiguration with elevated H3K9me2 and reduced H3K4me1, aligns with the overall downregulation of gene expression, underscoring the role of histone modifications in mediating transcriptional responses to lamin A loss.

Further, we compared the LAD genomic positioning among WT, *Sun1*KO, *Sun2*KO, and *Lmna*KO cells, and identified the similarity of their distribution in promoter regions and distal genomic areas, the LADs in *Sun2* KO and *Lmna* KO cells showed more similar changes in the decreased association with promoter regions and more distal intergenic areas (Fig.s 5G and 5H), and *Sun2* KO dramatically reduced lamin A expression, but minor effect in *Sun1* KO group (Fig. 5I),

Langtaosha (LTS) Preprint doi: https://doi.org/10.65215/ydw1ks77 This version posted November 19, 2025. The copyright holder for this preprint (which was not certified by peer review) is the author/funder. All Rights Reserved. No reuse allowed without permission.

indicating there are more functional correlations between SUN2 and lamin A, implying their hierarchical regulation of the SUN2-lamin A/C-LAD axis.

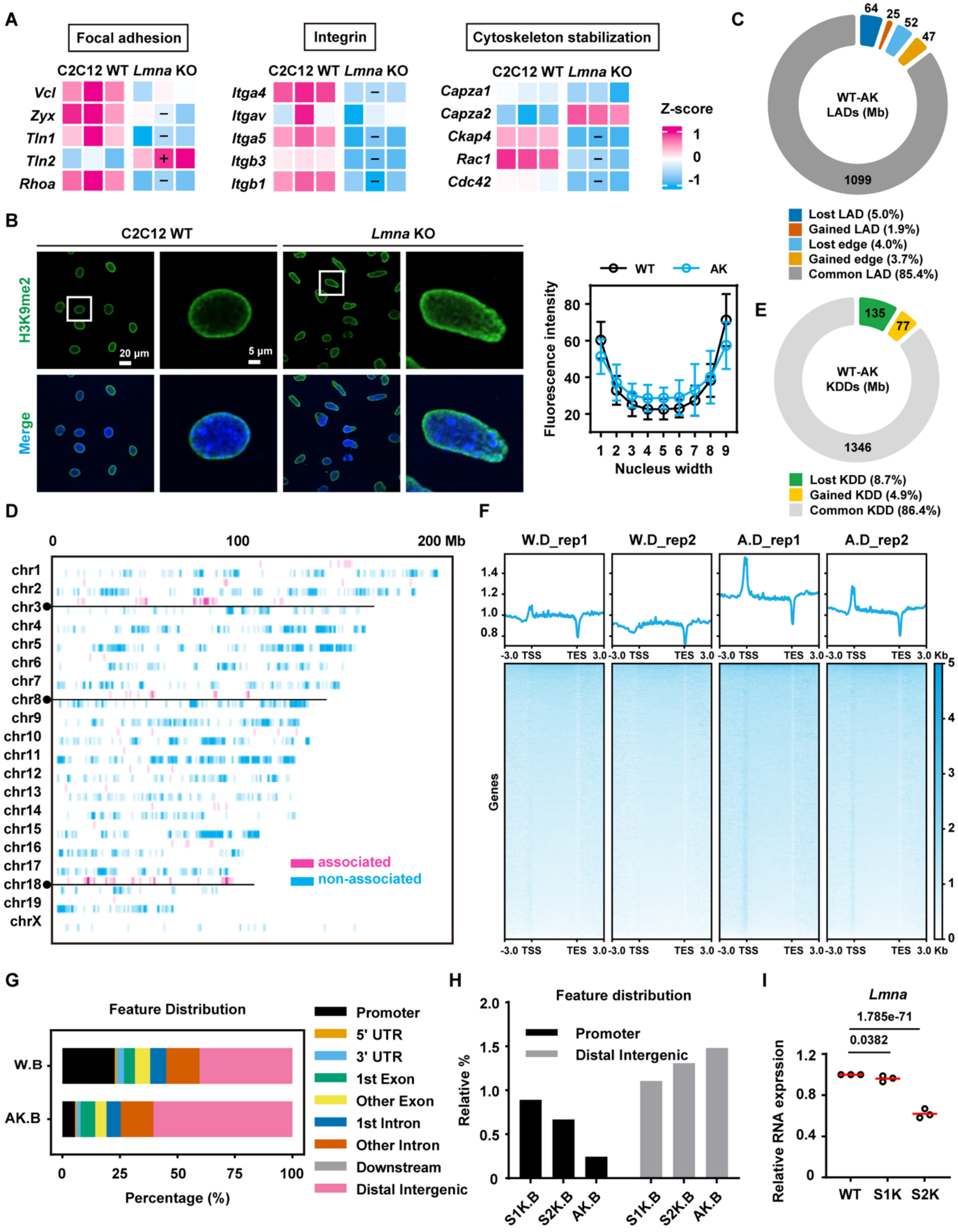

Langtaosha (LTS) Preprint doi: https://doi.org/10.65215/ydw1ks77 This version posted November 19, 2025. The copyright holder for this preprint (which was not certified by peer review) is the author/funder. All Rights Reserved. No reuse allowed without permission.

Fig. 5. *Lmna* knockout decreases cell adhesion genes expression and LAD regulation.

(A) The heatmap shows the relative expression levels of focal adhesion-related, integrin-related, and cytoskeleton-related genes in C2C12 WT, and *Lmna* KO cells (three biological replicates per group). Each row is standardized using the Z-score method. A “+” indicates significantly upregulated genes, and a “-” indicates significantly downregulated genes.

(B) Immunofluorescence staining and imaging of the nucleus and H3K9me2 in C2C12 WT and *Lmna* KO cells (H3K9me3, n = 23, 26 cells). Scale bar, 20 μm (left), 5 μm (right). Line graph showing H3K9me2 fluorescence distribution within nucleus. The x-axis divides the nuclear diameter into 9 equal parts. Data are presented as the mean with SD.

(C) Compared to C2C12 WT, the total length of five categories of LAD in *Lmna* KO cells (WT-AK) has changed, measured in Mb. The percentages on the legend represent the corresponding proportional changes.

(D) After knocking out *Lmna*, a heatmap shows significant changes in lamin B1 binding affinity at chromosomal locations. Red indicates regions with significantly increased binding affinity, while blue indicates regions with significantly decreased binding affinity.

(E) Compared to C2C12 WT, the total length of three classes of KDD in *Lmna* KO cells (WT-AK).

(F) The line graph above shows the total signal distribution of H3K9me2 across the entire genome and its up/downstream 3 kb regions in C2C12 WT and *Lmna* KO cells (two replicates per group). Below, the heatmap displays the H3K9me2 signal values around each gene, sorted from highest to lowest.

(G) Percentage distribution of gene characteristics associated with lamin B1 binding sites in C2C12 WT and *Lmna* KO cells. Gene characteristics include promoters, UTRs, exons, introns, and distal intergenic regions, among others.

(H) Relative percentage distribution of gene characteristics associated with lamin B1 binding sites in *Sun1* KO, *Sun2* KO and *Lmna* KO cells compared to C2C12 WT cells. The most altered gene characteristics were displayed including promoters and distal intergenic regions.

(I) Quantification of *Lmna* RNA transcription levels across the three cell groups in RNA-seq data. Each dot represents a biological replicate, and red line segments indicate the mean values.

W.D represents H3K9me2 binding sites in C2C12 WT cell, AK.B represents lamin B1 binding sites in *Lmna* KO cell, S1K.B represents lamin B1 binding sites in *Sun1* KO cell, and S2K.B represents lamin B1 binding sites in *Sun2* KO cell in all the figures.

SUN1/2 and their direct downstream protein lamin A/C prime myogenic differentiation

During the differentiation process from myoblasts to mature muscle fibers[50], cells need to respond to various mechanical cues such as intercellular traction and substrate stiffness to successfully

Langtaosha (LTS) Preprint doi: https://doi.org/10.65215/ydw1ks77 This version posted November 19, 2025. The copyright holder for this preprint (which was not certified by peer review) is the author/funder. All Rights Reserved. No reuse allowed without permission.

form multinucleated myotubes[51], and the force transmission into the nucleus is critical. To investigate the role of nuclear mechanotransductor proteins SUN1 and SUN2 in muscle cell fate determination, we induced differentiation in C2C12 cells for 6 days and evaluated myotube formation efficiency via heavy chain staining of MYH4 (Fig. 6A). WT C2C12 showed regular Myosin striped structures (myotubes), and on average, approximately 15.45% of the total cell population participated in fusion events to form myotubes (Fig. 6B). Among these, multinucleated myotubes (containing more than three nuclei) accounted for 45.27% of the fused structures (Fig. 6C). Knockout of either *Sun1* or *Sun2* severely impaired myogenic fusion. The average proportion of fused myotubes dropped dramatically to 0.17% and 0.26%, respectively, and the formation of multinucleated myotubes was completely abolished. These results demonstrate that SUN1 and SUN2 are essential for myotube differentiation in C2C12 cells, and their loss abrogates the capacity of myoblasts to undergo myogenesis.

Given that SUN proteins are known to interact with lamin A/C via their N-terminal domains [19], and considering that lamin A/C directly associates with LADs to influence chromatin organization and gene expression[52], we proposed that lamin A/C may serve as a critical downstream mediator through which SUN proteins exert regulatory control over LAD organization. To investigate whether lamin A/C participates in the hierarchical regulation axis of SUN1/2-LAD, we first performed immunofluorescence staining for lamin A/C in C2C12 WT, *Sun1*KO, and *Sun2* KO cells. We observed a redistribution of lamin A/C away from the nuclear periphery following the knockout of either *Sun1* or *Sun2* (Fig.s S11A-S11C), but there was no significant change in total protein levels of lamin A, lamin C, or total lamin A/C (Fig.s S11D-S11G), suggesting that SUN1/2 deficiency specifically disrupts the subnuclear localization of lamin A/C rather than its expression.

Then, using NanaPPI technology[53] to quantitatively measure protein-protein interaction, the verification results showed that the physical interaction between SUN2 and lamin A/C is greater than that between SUN1 and lamin A/C (Fig.s 6D and 6E). Moreover, SUN1 depletion markedly weakened the SUN2–lamin A/C interaction, whereas SUN2 deficiency had no substantial effect on the SUN1–lamin A/C interaction (Fig. 6F), revealing an asymmetric functional dependency within this mechanotransductory axis. To further investigate the effect of the nuclear skeleton protein lamin A/C on the fate of myoblasts, we induced *Lmna* knockout C2C12 cells into myogenic differentiation for six days. Compared to WT cells, *Lmna*KO cells completely failed to form multinucleated myotubes (Fig.s 6G and 6H), indicating a total loss of myogenic differentiation capacity. This underscores the essential role of lamin A/C in mediating myoblast fusion and fate determination.

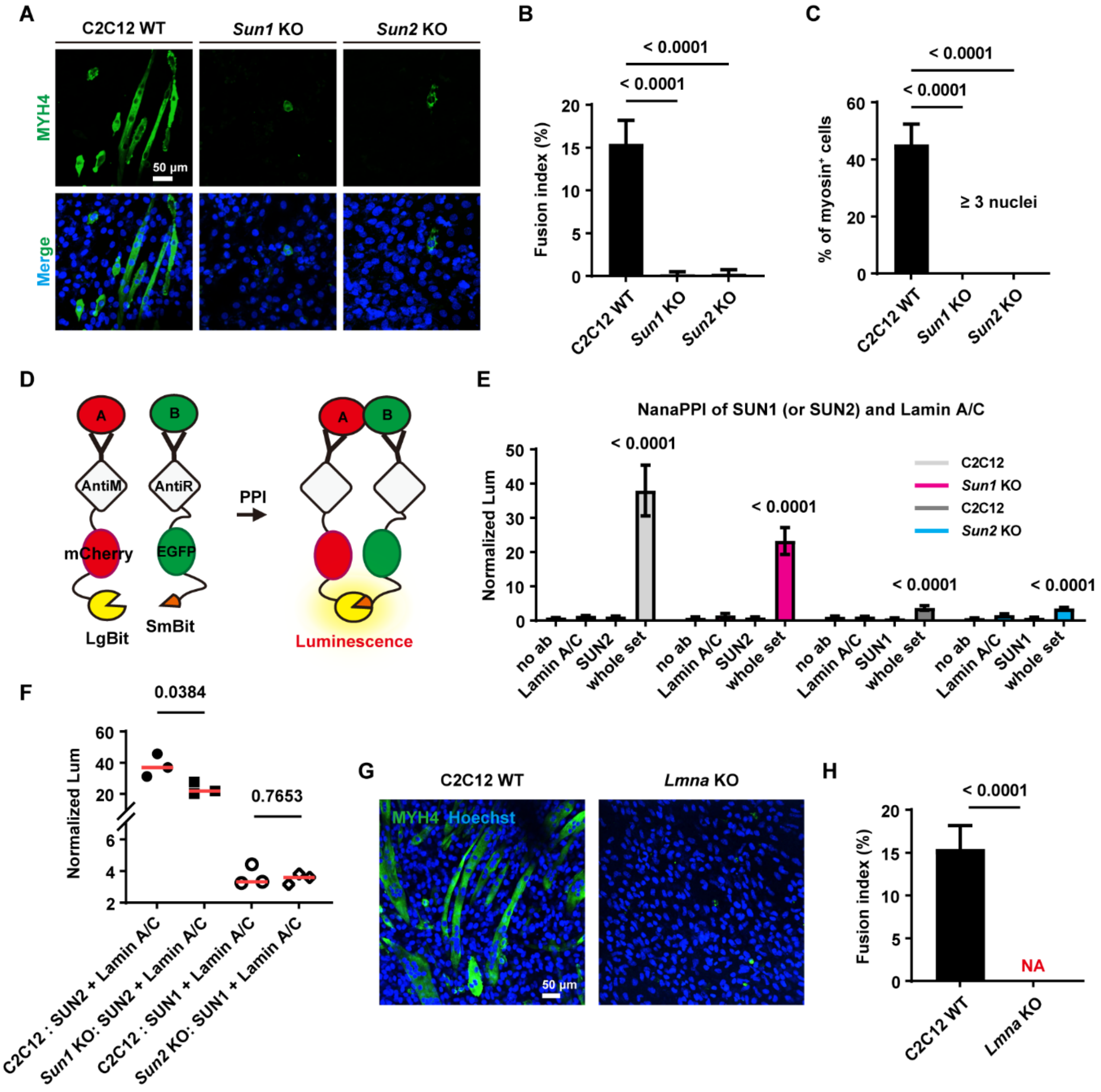

Fig. 6. Loss of cell differentiation function after knocking out of *Sun1*, *Sun2* or the downstream *Lmna*.

(A) Immunofluorescence staining and imaging of nuclei and MYH4 in C2C12 WT, *Sun1* KO, and *Sun2* KO cells (n = 5, 5, 5 views). Scale bar, 50 μm.

(B) Quantitative analysis of the ratio of fused myotube nuclei to total nuclei in each group. Data are presented as the mean with SD. One-way ANOVA.

(C) Quantitative analysis of the ratio of nuclei within individual myotubes (nuclei count > 3) to total nuclei across all myotubes. Data are presented as the mean with SD. One-way ANOVA.

(D) Schematic diagram of NanaPPI design.

(E) Quantitative analysis of the interaction between lamin A/C and SUN1 or SUN2 protein, after *Sun2* or *Sun1* knockout, respectively. Three biological replicates per group. Data are presented as the mean with SD. Two-tailed unpaired Student *t*-tests.

(F) Quantitative analysis of differences in protein interactions. The x-axis represents different PPI pairs across cells. Each dot represents a biological replicate, the red line segment represents the mean value. Two-tailed unpaired Student *t*-tests.

(G) Immunofluorescence staining and imaging of nuclei and MYH4 in C2C12 WT and *Lmna* KO cells (n = 5, 5 fields). Scale bar, 50 μm.

(H) Quantitative analysis of the proportion of nuclei in fused myotubes relative to total nuclei across each group. Data are presented as the mean with SD. Two-tailed unpaired Student *t*-tests.

Discussion

To elucidate whether regulating nuclear mechanotransduction modulates upstream mechanical signaling, this study reveals the role of SUN proteins in nuclear mechanoadaptation: reducing SUN proteins inhibit upstream mechanosensitive gene expression through LAD reorganization and chromatin remodeling, establishing a nuclear mechanical feedback loop. We discovered that: (1) SUN deficiency more severely disrupts mechanosensing and mechanotransduction in high-stiffness cells, e.g., C2C12 cells; (2) SUN1/2 is essential for maintaining nuclear-cytoskeletal integrity; and (3) SUN2 and lamin A/C cooperatively regulate adhesion-related genes via LAD dynamics and histone modifications.

Mechanical feedback defines as regulatory loops where mechanical cues modulate gene expression to facilitate adaptation to mechanical microenvironment[1, 16, 17], however, the core mechanotransduction axis mediating this process remains poorly characterized. In this study, by integrating RNA-seq data with functional observations, we demonstrate that stiffer C2C12 cells exhibit more severe mechanosensing deficits upon SUN1/2 depletion. We also delineate distinct roles for SUN1 and SUN2: SUN1 deficiency causes disordered F-actin alignment, while SUN2 loss leads to a reduction in F-actin content, suggesting roles in stabilizing versus dynamically responding to mechanical inputs. Recent studies have shown that SUN1 is essential for proper cytoskeletal force generation and focal adhesion maturation, linking the nucleus to mechanosensing (via integrin β1, vinculin, zyxin)[23, 54]. Destruction of actin results in a complete and irreversible disassembly of FA[55], consistent with the decomposition of FA after *Sun1/2* knockout. Additionally, SUN1 and SUN2 are vital for RhoA/ROCK-mediated actomyosin activity in vascular smooth muscle cells, indicating a potential feedback circuit between cytoskeletal tension and nuclear components[56]. Collectively, our findings provide a novel paradigm: nuclear mechanotransduction proteins (SUN1/2) modulate cellular mechanoadaptation by establishing a mechano-feedback loop that transcriptionally regulates upstream mechanosensitive genes.

Langtaosha (LTS) Preprint doi: https://doi.org/10.65215/ydw1ks77 This version posted November 19, 2025. The copyright holder for this preprint (which was not certified by peer review) is the author/funder. All Rights Reserved. No reuse allowed without permission.

Compared with controls, Calyculin A (CalyA)-treated C2C12 cells exhibited reduced both cell and nuclear area, along with a significant decrease in FA size. These findings suggest that CalyA enhances actomyosin contractility, accelerating FA turnover and resulting in smaller FAs[57] , likely dependent on Calyculin-A treatment concentration and duration[58]. While cells typically maintain mechanical homeostasis via feedback mechanisms that preserve force equilibrium under perturbation[56], SUN-deficient cells fail to respond to actin contractility, indicating loss of adaptive capacity.

Mechanical signaling extends beyond cytoskeletal remodeling into the spatial regulation of chromatin and lamina-associated domains[52, 59]. Our results align with studies showing that perturbation of nuclear envelope proteins disrupts LAD organization and heterochromatin distribution[46, 60]. Critically, we demonstrate that the LADs in *Sun2*KO and *Lmna*KO cells showed more similar changes in the decreased association with promoter regions and more distal intergenic areas, and *Sun2*KO reduced lamin A expression significantly but minor effect in *Sun1*KO cells. Together, these findings identify a SUN2-lamin A -LAD axis as a nuclear mechanical feedback pathway tuning adhesion gene expression.

In summary, SUN1/2 are critical regulators of nuclear mechanotransduction and cellular mechanical adaptation. By maintaining nuclear-cytoskeletal connectivity, SUN1/2 preserve LAD organization and adhesion gene expression, enabling dynamic mechanosensitivity adjustment to extracellular forces. The SUN1/2-dependent mechano-feedback loop highlights how the nucleus itself calibrates cellular responses to mechanical stress, preventing maladaptive outcomes such as adhesion loss and impaired mechanosensitivity. These insights not only expand our understanding of nuclear mechanics but also provide a framework to investigate how dysregulated nuclear feedback contributes to pathological states, including laminopathies and muscle disorders. Targeting SUN1/2-mediated nuclear feedback may represent a promising strategy for restoring mechanical resilience in disease contexts.

Langtaosha (LTS) Preprint doi: https://doi.org/10.65215/ydw1ks77 This version posted November 19, 2025. The copyright holder for this preprint (which was not certified by peer review) is the author/funder. All Rights Reserved. No reuse allowed without permission.

Materials and Methods C2C12 knockout cell lines

C2C12 were grown in DMEM (Gibco) supplemented with 10% fetal bovine serum (Sigma) and 1% penicillin-streptomycin (Gibco). For *Sun1*, *Sun2* and *Lmna* knockout cell lines, two sgRNAs targeting gene exons (*Sun1*: GTCCCGCCGCAGCTTGCGTCTGG and TAATGTGCGAATCAATAGCCTGG; *Sun2*: CACAGACTCGCTGTAGTAGGAGG and GGACAGGTGCTTCATGTTGCTGG; *Lmna*: GCGAGCTCCATGACCTGCGG and TCTCAGTGAGAAGCGCACAT) were designed using CCTop Wab (http://crispr.cos.uni-heidelberg.de) and cloned into the pX458-Cas9-GFP vector (Addgene #48138). C2C12 cells were transfected with the sgRNA plasmids using Lipofectamine™ 3000 (Thermo Scientific). GFP-positive cells were sorted by FACS at 48 hours post-transfection and single cells were expanded clonally. Knockout was verified by Sanger sequencing, western blot and immunofluorescence.

Myogenic differentiation

C2C12 cell lines were cultured upon reaching 90% confluency and induced to differentiate by addition of DMEM with 2% horse serum (Gibco #26050088). Differentiation media was replaced every 24 hours for the first 72 hours, and subsequently every 12 hours thereafter. After six days of differentiation, immunofluorescence staining was performed to evaluate Myosin expression and localization.

Calyculin A treatment

Cells were cultured for 12 hours and added Calyculin A (1 nM in DMSO, Cell Signaling 9902) for 20 minutes. Immunofluorescence staining was performed to evaluate Vinculin density.

Immunofluorescence

Cells were fixed with 4% paraformaldehyde for 15 minutes at room temperature, permeabilized with 0.25% Triton X-100 for 30 minutes and blocked in PBST containing 5% BSA for 2 hours. Cells were then incubated with primary antibodies diluted in PBST containing 1% BSA overnight at 4°C, followed by wash with PBST three times. Cells were then incubated with secondary antibodies for 1 hour at room temperature, followed by wash with PBST three times. Samples were incubated with Hoechst 33342 (1:1000, Cell Signaling 4082S) for 10 minutes to stain the nucleus. After washing by PBST twice, confocal imaging was performed in a Dragonfly Confocal Microscopy System (Seven-laser).

Primary antibodies included: TRITC Phalloidin (1:200, Biosharp BL1189A), H3K9me3 (1:500, Abcam ab8898), H3K9me2 (1:500, Active Motif 39239), H3K4me1 (1:500, Abcam ab8895), Lamin B1 (1:500, Santa Cruz sc-374015), Lamin A/C (1:500, Cell Signaling 4777), Myosin 4 (1:100, eBioscience 14-6503-82), Vinculin (1:200, Sigma-Aldrich V9264). Secondary antibodies included: anti-Rabbit Alexa 488 (1:2000, Cell Signaling 4412S), anti-Mouse Alexa 594 (1:2000, Cell Signaling 8890S), anti-Mouse Alexa 488 (1:2000, Cell Signaling 4408S).

Nanobody-assisted nanoluciferase fragment complementation for in situ measurement and visualization of endogenous protein-protein interaction (NanaPPI)

Langtaosha (LTS) Preprint doi: https://doi.org/10.65215/ydw1ks77 This version posted November 19, 2025. The copyright holder for this preprint (which was not certified by peer review) is the author/funder. All Rights Reserved. No reuse allowed without permission.

A 96-well plate was coated with fibronectin and incubated at 37 ℃ for 4 hours. Cells were seeded at 20,000 cells per well and cultured for 12 hours. Cells were fixed with 4% PFA for 30 minutes. Permeabilization was carried out using 0.25% Triton X-100 for 30 minutes. Cells were then blocked with 5% BSA in PBST for 2 hours. Primary antibody diluted in 1% BSA was added and incubated overnight at 4 ℃. Then, cells washed with PBST three times and incubated with secondary antibody (50 nM in 1% BSA with 1 mM DTT) for 1 hour. Cells were washed with PBST and stained with 0.1% propidium iodide (PI) for 10 minutes. After washing by PBST twice, the PI intensity was read by microplate reader (Ex/Em = 535/617 nm, BioTek Synergy H1). Pre-diluted substrates (Nano-Glo® Live Cell Assay System) were prepared in advance and added per well for luminescence detection (BioTek Synergy H1).

Primary antibodies included: Lamin A/C (1:500, Active Motif 39287), SUN1 (1:200, Abcam ab10302), SUN2 (1:300, Abcam ab124916). Secondary antibodies included: anti-Rabbit SB128-GFP-IgG + anti-Mouse LG-mCherry-IgG2a[53].

Western blot

Protein extraction was performed using RIPA lysis buffer. Then, the samples were separated by 10% SDS-PAGE and transferred to an ImmobilonFL PVDF membrane (Millipore #IPVH00010). Membranes were blocked with 5 % non-fat milk in PBST for 2 hours at room temperature and incubated with primary antibodies (Integrin alpha 4, 1:1000, Cell Signaling 8440S; Lamin A/C, 1:1000, Cell Signaling 4777; GAPDH, 1:5000, Cell Signaling 2118) overnight at 4 ℃. After washing with PBST, membranes were incubated with corresponding horseradish peroxidase (HRP)-conjugated secondary antibodies (anti-Mouse, 1:5000, Cell Signaling 7076; anti-Rabbit, 1:10000, Cell Signaling 7074) for 1 hour at room temperature. Finally, the signals were visualized using the Omni-ECL Femto Light Chemiluminescence Kit (Epizyme), and a ChemiDoc MP Imaging System (Bio-Rad). ImageJ software was utilized to analyze western blot data.

Quantitative real-time PCR (qPCR)

Total RNA was extracted with the Total RNA Kit I (Omega R6834) in accordance with the manufacturer’s protocol. Subsequently, 500 µg of RNA was reverse-transcribed into cDNA per reaction using random primers and Reverse Transcriptase (Takara RR036A). PCR was conducted on an MX3000P Stratagene system with Hieff® qPCR SYBR Green Master Mix (Yeasen 11204ES08) and gene-specific primers. Gene expression levels were normalized to GAPDH as an endogenous control. The primer sequences used were: GAPDH: Forward 5’-CAGAAGACTGTGGATGGCCC-3’, Reverse 5’-ATCCACGACGGACACATTGG-3’; Itga4: Forward 5’-GGTCCCAGGCTACATCGTTTT-3’, Reverse 5’-GGGGTAAGGATGTCTCGCAC-3’.

RNA-sequencing and analysis

Total RNA was isolated from C2C12, *Sun1* KO, *Sun2* KO and *Lmna* KO cells using the Total RNA Kit I and processed for Illumina library preparation. The mRNA samples were sequenced on DNBSEQ-T7 platform with 150 bp paired-end. Raw reads were first preprocessed using Ktrim

Langtaosha (LTS) Preprint doi: https://doi.org/10.65215/ydw1ks77 This version posted November 19, 2025. The copyright holder for this preprint (which was not certified by peer review) is the author/funder. All Rights Reserved. No reuse allowed without permission.

v1.3.0 to remove sequencing adapters and low-quality reads. Then, clean reads were aligned to mm10 reference genome using STAR v2.7.3a. Transcript abundance was estimated using featureCounts tools from Subread v2.0.1 against ENSEMBL gene annotation v102. Differential expression gene (DEG, FDR < 0.05 and Fold Change ⩾ 1.2) was determined using DESeq2 v1.30.0. Functional annotation was performed using the DAVID website.

Data of THP-1, HUVEC, CT26 and adipogenic cells were downloaded from the Gene Expression Omnibus (GSE85022, GSE213099, GSE250602, GSE193505).

Cleavage under targets and tagmentation (CUT&Tag)

Sun1 KO, *Sun2* KO or *Lmna* KO C2C12 cells were subjected to perform CUT&Tag assay as previously described[61] by Hieff NGS® G-Type In-Situ DNA Binding Profiling Library Prep Kit for Illumina (Yeasen 12598ES12) according to the manufacturer's instructions. In brief, 100,000 cells were harvested and washed twice, then incubated with activated Concanavalin A coated magnetic beads. Primary antibody (Lamin B1, Abcam ab10648; H3K9me2, Active Motif 39239; H3K4me1, Abcam ab8895) diluted 1:50 in blocking buffer was added and incubated on a rotating platform at 4℃ overnight. Then, Guinea Pig anti-Rabbit secondary antibody (ABIN101961) diluted 1:50 in blocking buffer was added and incubated for 1 hour. After washing, cells were segmented with pA/G-Tn5 transposase at 37℃ for 1 hour. After 30 minutes incubation with proteinase K at 55℃, DNA was extracted and the libraries were prepared through PCR. Libraries were quantified, quality assessed and sequenced by Qubit 4.0, Agilent 4200 Bioanalyzer and Illumina NovaSeq X platform.

CUT&Tag analysis

Raw reads were aligned to mm10 genome using Bowtie2 v0.7.17, and then converted to sam format. Sam files were then filtered using samtools v1.7, sorted and converted to bam format. PCR duplicates were removed using Mark-Duplicates program in Picard tools. Replicate bigwig coverage tracks were made using Deeptools v3.1.1 bamCoverage. Log2 transformed tracks are shown using a genome browser (Integrative Genomic Viewer). Top 1% peaks were called using SEACR with default settings. Samtools merge was used to combine biological replicate bam files. LAD, KDD and KMD were called using EDD v1.1.18 with paired merged CUT&Tag and IgG bam files. LAD/KDD/KMD PCA analysis was performed using princomp function in R's stats package. Resulting peak files, along with paired replicate bam files, were input into DiffBind for differential binding analysis using FDR < 0.1 as significance threshold and annotated using ChIPseeker v1.36.0.

Statistical analysis

For image processing, images were analyzed using Imaris v9.9. Fluorescence intensity was measured using Image-Pro Plus, NIS-Elements or ImageJ software. Data are presented as Mean ± SD and were calculated using GraphPad Prism v9.5. Between-group differences were assessed using unpaired two-tailed Student *t*-tests or one-way ANOVA, with a *P*-value < 0.05 considered statistically significant. Statistical methods are indicated in Figure legends.

Langtaosha (LTS) Preprint doi: https://doi.org/10.65215/ydw1ks77 This version posted November 19, 2025. The copyright holder for this preprint (which was not certified by peer review) is the author/funder. All Rights Reserved. No reuse allowed without permission.

Acknowledgments

This work was financially supported by the National Natural Science Foundation of China (12572355 and 12372302 to J.Q., 32471370 to Q.P.), the Guangdong Pearl River Talent Program (2021QN02Y781 to Q.P.) and the Natural Science Foundation of Chongqing (No. CSTB2023NSCQ-MSX0918 to J.Q.)

Author Contributions

Describe the contributions of each author to the paper.

Yafan Xie: Data curation; Formal analysis; Methodology; Validation; Visualization; Writing—original draft; Writing—review and editing.

Zhaoyan Zuo: Data curation; Formal analysis; Validation; Visualization.

Yanjing Zhao: Formal analysis

Liping Guo: Formal analysis

Wei Xu：Formal analysis

Juhui Qiu: Conceptualization; Funding acquisition; Supervision; Methodology; Writing—review and editing.

Qin Peng: Conceptualization; Funding acquisition; Supervision; Methodology; Writing—review and editing.

Competing interests: The authors declare no competing interests.

References

[1] WU M, YANG H, LIU S, et al. Enhanced engraftment of human haematopoietic stem cells via mechanical remodelling mediated by the corticotropin-releasing hormone [J]. Nat Biomed Eng, 2025, 9(5): 754-71.

[2] ALISAFAEI F, SHAKIBA D, HONG Y, et al. Tension anisotropy drives fibroblast phenotypic transition by self-reinforcing cell-extracellular matrix mechanical feedback [J]. Nat Mater, 2025, 24(6): 955-65.

[3] NAVA M M, MIROSHNIKOVA Y A, BIGGS L C, et al. Heterochromatin-Driven Nuclear Softening Protects the Genome against Mechanical Stress-Induced Damage [J]. Cell, 2020, 181(4): 800-17 e22.

[4] ECHARRI A. A Multisensory Network Drives Nuclear Mechanoadaptation [J]. Biomolecules, 2022, 12(3).

[5] PARK J E, JO J, XU K, et al. Attenuated Nuclear Tension Regulates Progerin-Induced Mechanosensitive Nuclear Wrinkling and Chromatin Remodeling [J]. Adv Sci (Weinh), 2025, 12(31): e2502375.

[6] KRSHNAN L, SIU W S, VAN DE WEIJER M, et al. Regulated degradation of the inner nuclear membrane protein SUN2 maintains nuclear envelope architecture and function [J]. Elife, 2022, 11.

[7] GOELZER M, HOWARD S, ZAVALA A G, et al. Depletion of SUN1/2 induces heterochromatin accrual in

Langtaosha (LTS) Preprint doi: https://doi.org/10.65215/ydw1ks77 This version posted November 19, 2025. The copyright holder for this preprint (which was not certified by peer review) is the author/funder. All Rights Reserved. No reuse allowed without permission.

mesenchymal stem cells during adipogenesis [J]. Commun Biol, 2025, 8(1): 428.

[8] LI T, QIU J, JIA T, et al. G3BP2 regulates oscillatory shear stress-induced endothelial dysfunction [J]. Genes Dis, 2022, 9(6): 1701-15.

[9] LI T, SAFITRI M, ZHANG K, et al. Downregulation of G3BP2 reduces atherosclerotic lesions in ApoE(-/-) mice [J]. Atherosclerosis, 2020, 310: 64-74.

[10] WEI F, XU X, ZHANG C, et al. Stress fiber anisotropy contributes to force-mode dependent chromatin stretching and gene upregulation in living cells [J]. Nat Commun, 2020, 11(1): 4902.

[11] HOFFMAN L M, SMITH M A, JENSEN C C, et al. Mechanical stress triggers nuclear remodeling and the formation of transmembrane actin nuclear lines with associated nuclear pore complexes [J]. Mol Biol Cell, 2020, 31(16): 1774-87.

[12] MU X, TSENG C, HAMBRIGHT W S, et al. Cytoskeleton stiffness regulates cellular senescence and innate immune response in Hutchinson-Gilford Progeria Syndrome [J]. Aging Cell, 2020, 19(8): e13152.

[13] HARADA T, SWIFT J, IRIANTO J, et al. Nuclear lamin stiffness is a barrier to 3D migration, but softness can limit survival [J]. J Cell Biol, 2014, 204(5): 669-82.

[14] JANOTA C S, CALERO-CUENCA F J, GOMES E R. The role of the cell nucleus in mechanotransduction [J]. Curr Opin Cell Biol, 2020, 63: 204-11.

[15] WALKER C J, CROCINI C, RAMIREZ D, et al. Nuclear mechanosensing drives chromatin remodelling in persistently activated fibroblasts [J]. Nat Biomed Eng, 2021, 5(12): 1485-99.

[16] DANG Y, LATTNER J, LAHOLA-CHOMIAK A A, et al. Self-propagating wave drives morphogenesis of skull bones in vivo [J]. Nat Commun, 2025, 16(1): 4330.

[17] HALLOU A, HE R, SIMONS B D, et al. A computational pipeline for spatial mechano-transcriptomics [J]. Nat Methods, 2025, 22(4): 737-50.

[18] LI MOW CHEE F, BEERNAERT B, GRIFFITH B G C, et al. Mena regulates nesprin-2 to control actin-nuclear lamina associations, trans-nuclear membrane signalling and gene expression [J]. Nat Commun, 2023, 14(1): 1602.

[19] BOUGARAN P, BAUTCH V L. Life at the crossroads: the nuclear LINC complex and vascular mechanotransduction [J]. Front Physiol, 2024, 15: 1411995.

[20] DUPONT S, WICKSTRÖM S A. Mechanical regulation of chromatin and transcription [J]. Nat Rev Genet, 2022, 23(10): 624-43.

[21] KALUKULA Y, STEPHENS A D, LAMMERDING J, et al. Mechanics and functional consequences of nuclear deformations [J]. Nat Rev Mol Cell Biol, 2022, 23(9): 583-602.

[22] YUE X, CUI J, SUN Z, et al. Nuclear softening mediated by Sun2 suppression delays mechanical stress-induced cellular senescence [J]. Cell Death Discov, 2023, 9(1): 167.

[23] UEDA N, MAEKAWA M, MATSUI T S, et al. Inner Nuclear Membrane Protein, SUN1, is Required for Cytoskeletal Force Generation and Focal Adhesion Maturation [J]. Front Cell Dev Biol, 2022, 10: 885859.

[24] SHIRAISHI K, SHAH P P, MORLEY M P, et al. Biophysical forces mediated by respiration maintain lung alveolar epithelial cell fate [J]. Cell, 2023, 186(7): 1478-92.e15.

[25] DHANKHAR M, GUO Z, KANT A, et al. Revealing the biophysics of lamina-associated domain formation by integrating theoretical modeling and high-resolution imaging [J]. Nat Commun, 2025, 16(1): 7909.

[26] HEO S J, THAKUR S, CHEN X, et al. Aberrant chromatin reorganization in cells from diseased fibrous connective tissue in response to altered chemomechanical cues [J]. Nat Biomed Eng, 2023, 7(2): 177-91.

Langtaosha (LTS) Preprint doi: https://doi.org/10.65215/ydw1ks77 This version posted November 19, 2025. The copyright holder for this preprint (which was not certified by peer review) is the author/funder. All Rights Reserved. No reuse allowed without permission.

[27] PAL M, SCHAUER T, BURTON A, et al. The establishment of nuclear organization in mouse embryos is orchestrated by multiple epigenetic pathways [J]. Cell, 2025, 188(13): 3583-602.e21.

[28] WANG Y, ELSHERBINY A, KESSLER L, et al. Lamin A/C-dependent chromatin architecture safeguards naïve pluripotency to prevent aberrant cardiovascular cell fate and function [J]. Nat Commun, 2022, 13(1): 6663.

[29] SHAH P P, LV W, RHOADES J H, et al. Pathogenic LMNA variants disrupt cardiac lamina-chromatin interactions and de-repress alternative fate genes [J]. Cell Stem Cell, 2021, 28(5): 938-54 e9.

[30] SEN B, XIE Z, THOMAS M D, et al. Nuclear actin structure regulates chromatin accessibility [J]. Nat Commun, 2024, 15(1): 4095.

[31] GUO M, WONG I Y, MOORE A S, et al. Vimentin intermediate filaments as structural and mechanical coordinators of mesenchymal cells [J]. Nat Cell Biol, 2025, 27(8): 1210-8.

[32] KIRBY T J, LAMMERDING J. Emerging views of the nucleus as a cellular mechanosensor [J]. Nat Cell Biol, 2018, 20(4): 373-81.

[33] CHASTNEY M R, KAIVOLA J, LEPPÄNEN V M, et al. The role and regulation of integrins in cell migration and invasion [J]. Nat Rev Mol Cell Biol, 2025, 26(2): 147-67.

[34] WANG H, SAID R, NGUYEN-VIGOUROUX C, et al. Talin and vinculin combine their activities to trigger actin assembly [J]. Nat Commun, 2024, 15(1): 9497.

[35] SCHWARTZ M A. Cell biology. The force is with us [J]. Science, 2009, 323(5914): 588-9.

[36] JIAO S, LI C, GUO F, et al. SUN1/2 controls macrophage polarization via modulating nuclear size and stiffness [J]. Nat Commun, 2023, 14(1): 6416.

[37] BUGLAK D B, BOUGARAN P, KULIKAUSKAS M R, et al. Nuclear SUN1 stabilizes endothelial cell junctions via microtubules to regulate blood vessel formation [J]. Elife, 2023, 12.

[38] NASR S, LI L, ASAD M, et al. A computational pipeline for identifying gene targets and signalling pathways in cancer cells to improve lymphocyte infiltration and immune checkpoint therapy efficacy [J]. EBioMedicine, 2024, 104: 105167.

[39] RICHARDS C J, WIERENGA A T J, BROUWERS-VOS A Z, et al. Elastic properties of leukemic cells linked to maturation stage and integrin activation [J]. iScience, 2025, 28(4): 112150.

[40] LUO Q, KUANG D, ZHANG B, et al. Cell stiffness determined by atomic force microscopy and its correlation with cell motility [J]. Biochim Biophys Acta, 2016, 1860(9): 1953-60.

[41] WANG K, QIN Y, CHEN Y. In situ AFM detection of the stiffness of the in situ exposed cell nucleus [J]. Biochim Biophys Acta Mol Cell Res, 2021, 1868(5): 118985.

[42] SWIFT J, IVANOVSKA I L, BUXBOIM A, et al. Nuclear lamin-A scales with tissue stiffness and enhances matrix-directed differentiation [J]. Science, 2013, 341(6149): 1240104.

[43] ISHIHARA H, MARTIN B L, BRAUTIGAN D L, et al. Calyculin A and okadaic acid: inhibitors of protein phosphatase activity [J]. Biochem Biophys Res Commun, 1989, 159(3): 871-7.

[44] ITO-ISHIDA A, BAKER S A, SILLITOE R V, et al. MeCP2 Levels Regulate the 3D Structure of Heterochromatic Foci in Mouse Neurons [J]. J Neurosci, 2020, 40(45): 8746-66.

[45] SUN C, ZHAO Y, GUO L, et al. The interplay between histone modifications and nuclear lamina in genome regulation [J]. J Genet Genomics, 2025, 52(1): 24-38.

[46] MADSEN-ØSTERBYE J, ABDELHALIM M, BAUDEMENT M O, et al. Local euchromatin enrichment in lamina-associated domains anticipates their repositioning in the adipogenic lineage [J]. Genome Biol, 2022,

Langtaosha (LTS) Preprint doi: https://doi.org/10.65215/ydw1ks77 This version posted November 19, 2025. The copyright holder for this preprint (which was not certified by peer review) is the author/funder. All Rights Reserved. No reuse allowed without permission.

23(1): 91.

[47] SUN L, XIE Y, ZUO Z, et al. Decreasing Lamin A Triggers Cell Fate Transitions through Heterochromatin-Nuclear Periphery Detethering [J]. Biomater Res, 2025, 29: 0256.

[48] MARIN H C, ALLEN C, SIMENTAL E, et al. The nuclear periphery confers repression on H3K9me2-marked genes and transposons to shape cell fate [J]. Nat Cell Biol, 2025, 27(8): 1311-26.

[49] KUBO N, CHEN P B, HU R, et al. H3K4me1 facilitates promoter-enhancer interactions and gene activation during embryonic stem cell differentiation [J]. Mol Cell, 2024, 84(9): 1742-52.e5.

[50] BENARROCH L, MADSEN-ØSTERBYE J, ABDELHALIM M, et al. Cellular and Genomic Features of Muscle Differentiation from Isogenic Fibroblasts and Myoblasts [J]. Cells, 2023, 12(15).

[51] CHAL J, POURQUIÉ O. Making muscle: skeletal myogenesis in vivo and in vitro [J]. Development, 2017, 144(12): 2104-22.

[52] VAN STEENSEL B, BELMONT A S. Lamina-Associated Domains: Links with Chromosome Architecture, Heterochromatin, and Gene Repression [J]. Cell, 2017, 169(5): 780-91.

[53] LI Q, LIU H, DU X, et al. Nanobody-assisted nanoluciferase fragment complementation for in situ measurement and visualization of endogenous protein-protein interaction [J]. Biosens Bioelectron, 2025, 272: 117102.

[54] NARDONE G, OLIVER-DE LA CRUZ J, VRBSKY J, et al. YAP regulates cell mechanics by controlling focal adhesion assembly [J]. Nat Commun, 2017, 8: 15321.

[55] KOVALEVA A, SOLOMATINA E, TLEGENOVA M, et al. How Actin Polymerization and Myosin II Activity Regulate Focal Adhesion Dynamics in Motile Cells [J]. Int J Mol Sci, 2025, 26(16).

[56] PORTER L, MINAISAH R M, AHMED S, et al. SUN1/2 Are Essential for RhoA/ROCK-Regulated Actomyosin Activity in Isolated Vascular Smooth Muscle Cells [J]. Cells, 2020, 9(1).

[57] STRICKER J, ARATYN-SCHAUS Y, OAKES P W, et al. Spatiotemporal constraints on the force-dependent growth of focal adhesions [J]. Biophys J, 2011, 100(12): 2883-93.

[58] LEOPOLDT D, YEE H F, JR., ROZENGURT E. Calyculin-A induces focal adhesion assembly and tyrosine phosphorylation of p125(Fak), p130(Cas), and paxillin in Swiss 3T3 cells [J]. J Cell Physiol, 2001, 188(1): 106-19.

[59] BIEDZINSKI S, AGSU G, VIANAY B, et al. Microtubules control nuclear shape and gene expression during early stages of hematopoietic differentiation [J]. Embo j, 2020, 39(23): e103957.

[60] BRIAND N, COLLAS P. Lamina-associated domains: peripheral matters and internal affairs [J]. Genome Biol, 2020, 21(1): 85.

[61] KAYA-OKUR H S, WU S J, CODOMO C A, et al. CUT&Tag for efficient epigenomic profiling of small samples and single cells [J]. Nat Commun, 2019, 10(1): 1930.

Langtaosha (LTS) Preprint doi: https://doi.org/10.65215/ydw1ks77 This version posted November 19, 2025. The copyright holder for this preprint (which was not certified by peer review) is the author/funder. All Rights Reserved. No reuse allowed without permission.

SUPPLEMENTAL INFORMATION

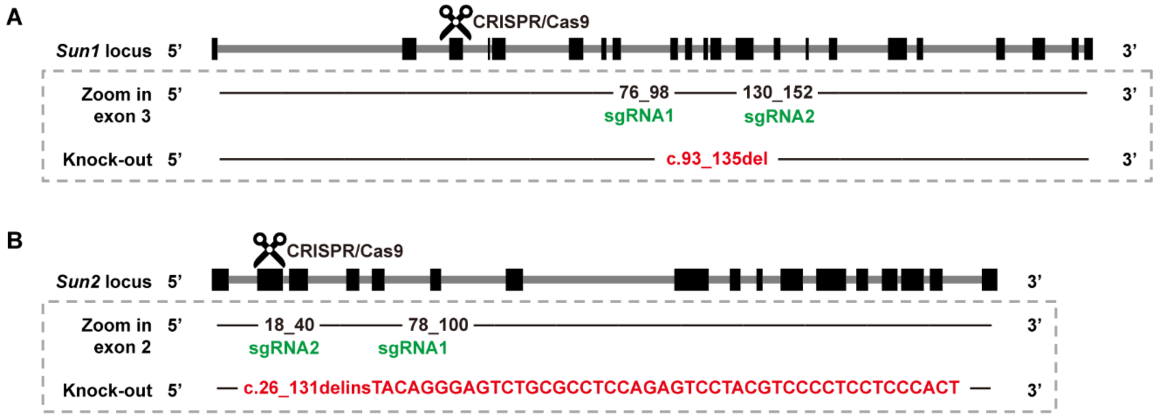

Supplementary Fig. S1. Schematic of *Sun1* and *Sun2* genes knockout in C2C12.

(A) Schematic diagram of *Sun1* gene knockout. Black blocks represent the exons of *Sun1*. Green indicates two sgRNA sequences targeting the exon 3 of *Sun1*. Red marks the deletion mutation sites.

(B) Schematic diagram of *Sun2* gene knockout. Black blocks represent the exons of *Sun2*. Green indicates two sgRNA sequences targeting the exon 2 of *Sun2*. Red marks the insertion and deletion mutation sites.

Langtaosha (LTS) Preprint doi: https://doi.org/10.65215/ydw1ks77 This version posted November 19, 2025. The copyright holder for this preprint (which was not certified by peer review) is the author/funder. All Rights Reserved. No reuse allowed without permission.

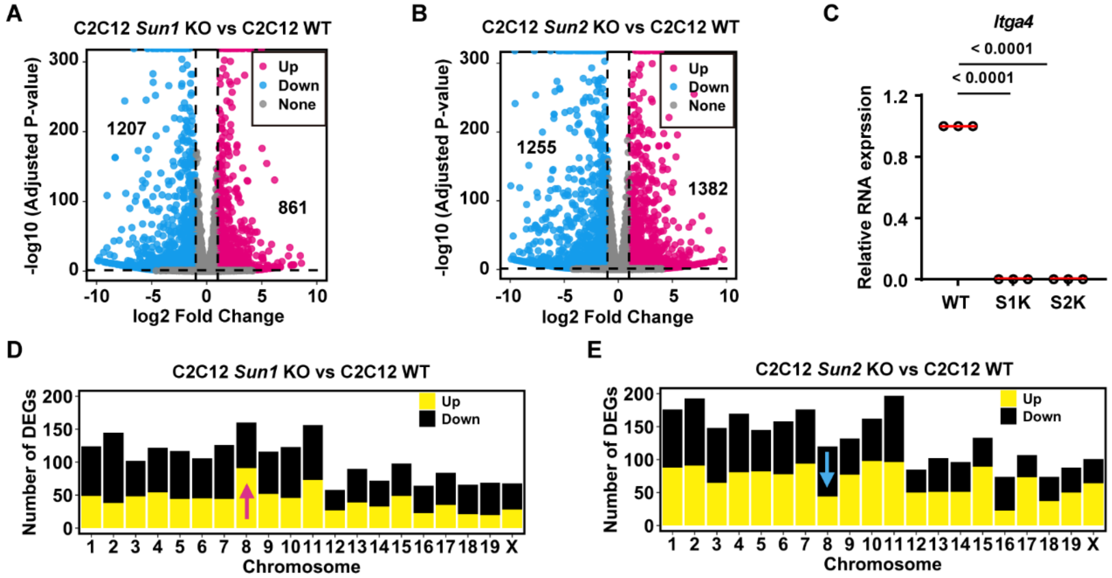

Supplementary Fig. S2. Loss of SUN1 or SUN2 affects downstream gene transcription and integrin α4 protein expression.

(A and B) Volcano plot showing differentially expressed genes in the *Sun1* KO group compared to the C2C12 WT group (A) and in the *Sun2* KO group compared to the C2C12 WT group (B) with three replicates per group. Each dot represents a gene. The black dashed lines indicate the thresholds for filtering DEG: FDR < 0.05 and Fold Change ⩾ 1.2. Red color indicates significantly upregulated genes, blue color indicates significantly downregulated genes, and gray indicates genes with no significant differences. The number of genes in each region is labeled accordingly.

(C) Quantification of integrin α4 RNA transcription levels across the three cell groups. Each dot represents a biological replicate, and red line segments indicate the mean values. One-way ANOVA.

(D and E) The number of DEGs on each chromosome after *Sun1* (D) or *Sun2* (E) knockout.

Langtaosha (LTS) Preprint doi: https://doi.org/10.65215/ydw1ks77 This version posted November 19, 2025. The copyright holder for this preprint (which was not certified by peer review) is the author/funder. All Rights Reserved. No reuse allowed without permission.

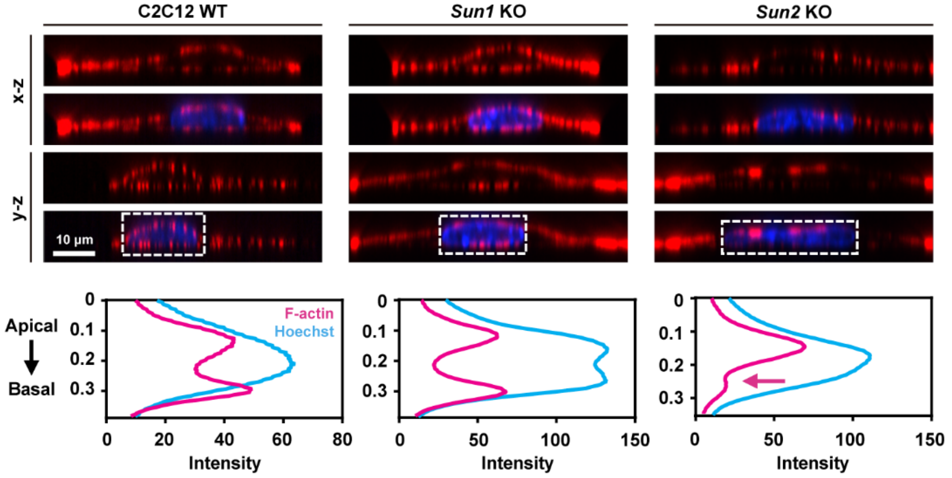

Supplementary Fig. S3. Alterations in C2C12 cell cytoskeleton and nuclear morphology after knocking out *Sun1* or *Sun2*.

Orthogonal views in the x-z and y-z planes, F-actin in red and nuclei in blue. Scale bar, 10 μm. The bottom graphs show quantitative fluorescence intensity profiles within the white boxed regions.

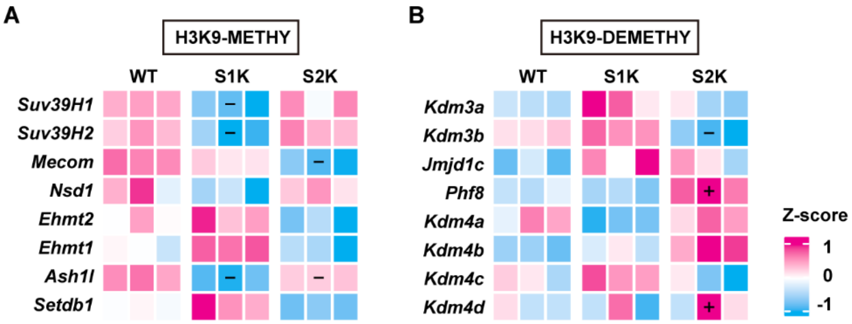

Supplementary Fig. S4. The heterochromatic state also changes after knocking out *Sun1/2*.

(A and B) The heatmap shows the expression change levels of H3K9 methylation-related (A) and H3K9 demethylation-related (B) genes in C2C12 WT, *Sun1* KO (S1K), and *Sun2* KO (S2K) cells (three replicates per group). Each row is standardized using the Z-score method. A "+" indicates significantly upregulated genes, and a "-" indicates significantly downregulated genes.

Langtaosha (LTS) Preprint doi: https://doi.org/10.65215/ydw1ks77 This version posted November 19, 2025. The copyright holder for this preprint (which was not certified by peer review) is the author/funder. All Rights Reserved. No reuse allowed without permission.

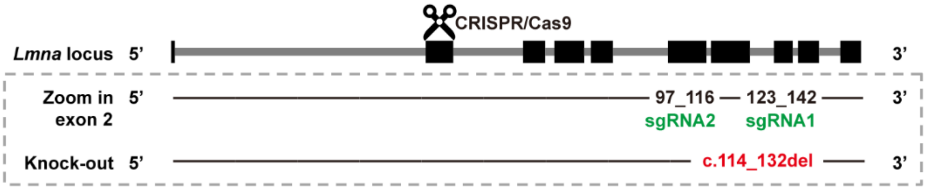

Supplementary Fig. S5. Schematic of *Lmna* gene knockout.

Black rectangles represent the exons of *Lmna*. Green indicates the two sgRNA sequences targeting the exon 2, while red marks the deletion mutation site.

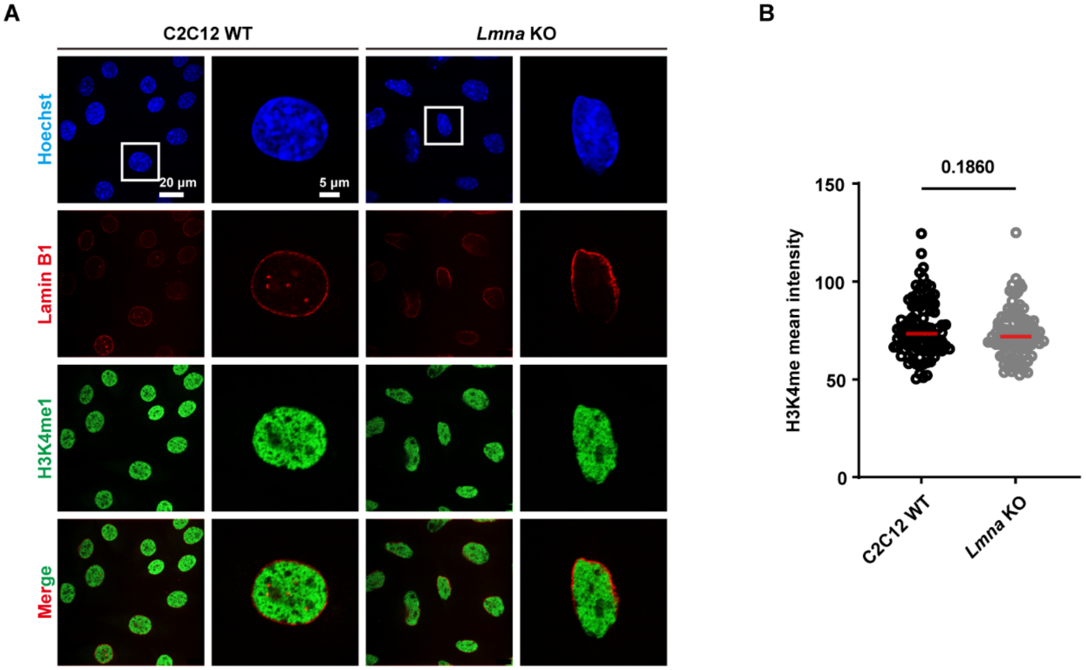

Supplementary Fig. S6. Lamin A/C loss causes perinuclear defects of lamin B1 but does not change the intensity of H3K4me1.

(A) Immunofluorescence staining and imaging of the nucleus, H3K4me1, and lamin B1 (H3K4me1, n = 95, 95 cells). Scale bar, 20 µm, 5 µm.

(B) Quantitative analysis of the average fluorescence intensity of H3K4me1. Each dot represents one cell, and the red line segment indicates the mean value. Two-tailed unpaired Student *t*-tests.

Langtaosha (LTS) Preprint doi: https://doi.org/10.65215/ydw1ks77 This version posted November 19, 2025. The copyright holder for this preprint (which was not certified by peer review) is the author/funder. All Rights Reserved. No reuse allowed without permission.

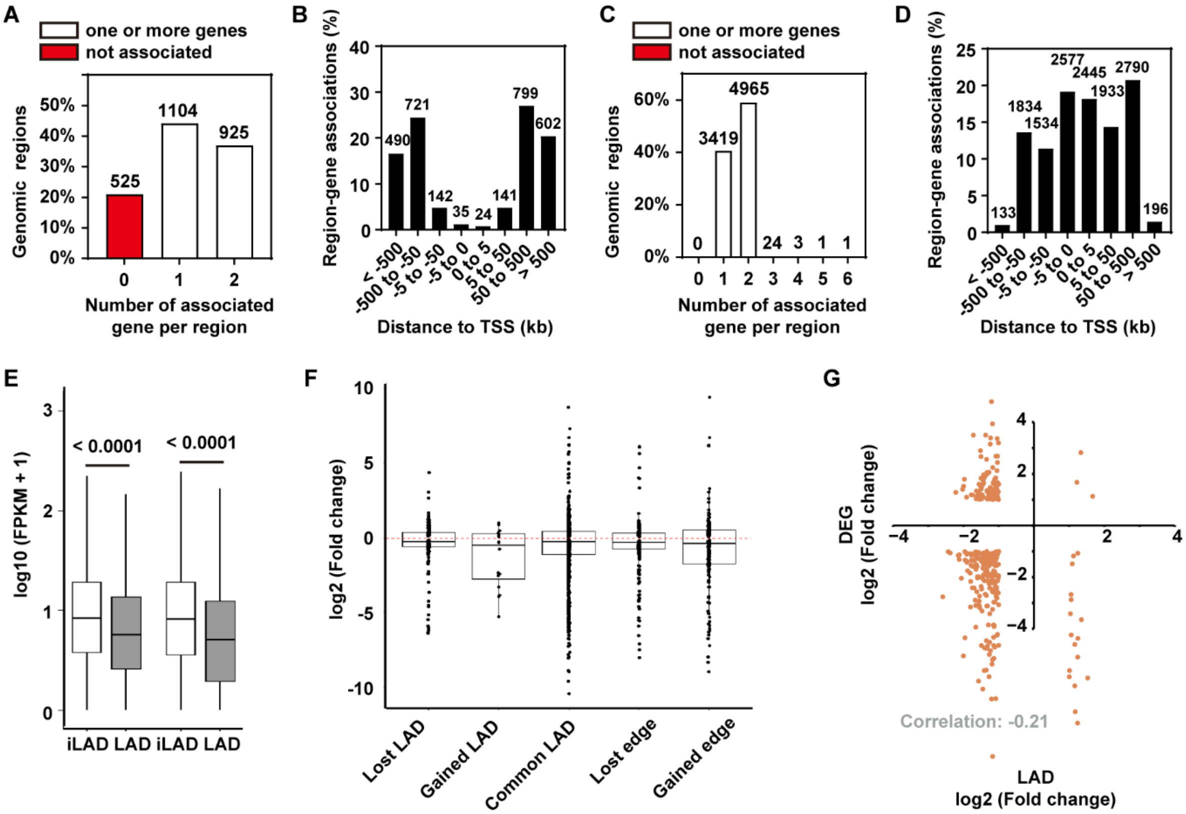

Supplementary Fig. S7. Alteration in gene characteristics of LAD after *Lmna* knockout.

(A) Bar chart showing the number of associated genes per sites with significantly increased lamin B1 binding affinity after *Lmna* knockout.

(B) Distance distribution plot showing the distance of each site from the nearest gene region in (A).

(C) Bar chart showing the number of associated genes per sites with significantly decreased lamin B1 binding affinity after *Lmna* knockout.

(D) Distance distribution plot showing the distance of each site from the nearest gene region in (C).

(E) Quantitative analysis of gene expression levels in LAD and i-LAD between C2C12 WT and *Lmna* KO cells. Data are presented as the mean with SD. Two-tailed unpaired Student *t*-tests.

(F) Quantitative analysis of gene expression change fold in the five classes of LAD. Data are presented as the mean with SD. Each dot represents a LAD, and red line segments indicate the 0 values.

(G) The quadrant plot displays genes with significant changes in lamin B1 affinity (LAD) and genes with significant changes in transcriptional expression (DEG).

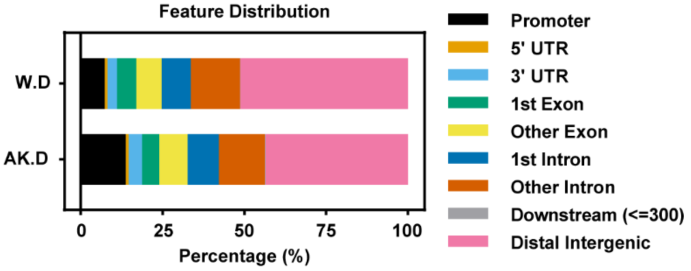

Supplementary Fig. S8. The proportion of H3K9me2 binding in promoter region increases after *Lmna* knockdown.

Percentage distribution of gene characteristics associated with H3K9me2 binding sites in C2C12 WT and *Lmna* KO cells. Gene characteristics include promoters, UTRs, exons, introns, and distal intergenic regions, among others. W.D represents H3K9me2 binding sites in C2C12 WT, and A.D represents H3K9me2 binding sites in *Lmna* KO cell.

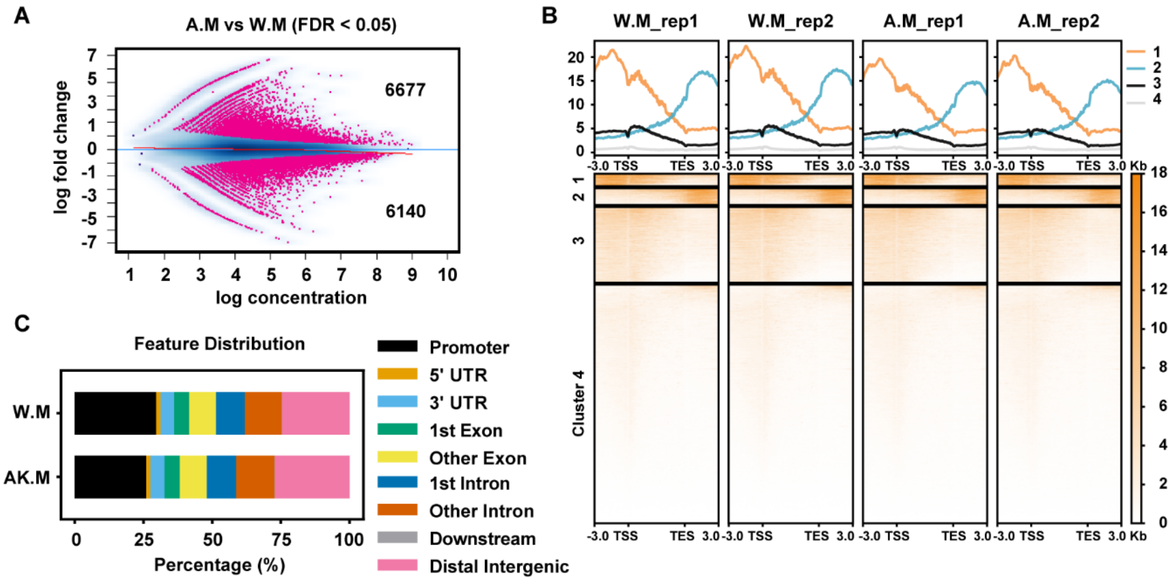

Supplementary Fig. S9. The proportion of H3K4me1 binding in promoter region decreases after *Lmna* knockout.

(A) The Bland-Altman plot illustrates the H3K4me1 binding sites with significant changes in affinity after *Lmna* knockout. Each dot represents a site. The number of sites in each region is

Langtaosha (LTS) Preprint doi: https://doi.org/10.65215/ydw1ks77 This version posted November 19, 2025. The copyright holder for this preprint (which was not certified by peer review) is the author/funder. All Rights Reserved. No reuse allowed without permission.

labeled accordingly.

(B) The line graph above shows the signal distribution of H3K4me1 across the entire genome and its up/downstream 3 kb regions in C2C12 WT and *Lmna* KO cells (two replicates per group). The total signals were clustered into four categories. Below, the heatmap displays the H3K4me1 signal values around each gene within each cluster, sorted from highest to lowest.

(C) Percentage distribution of gene characteristics associated with H3K4me1 binding sites in C2C12 WT and *Lmna* cells. Gene characteristics include promoters, UTRs, exons, introns, and distal intergenic regions, among others.

W.M represents H3K4me1 binding sites in C2C12 WT, and A.M represents H3K4me1 binding sites in *Lmna* KO cell in all the figures.

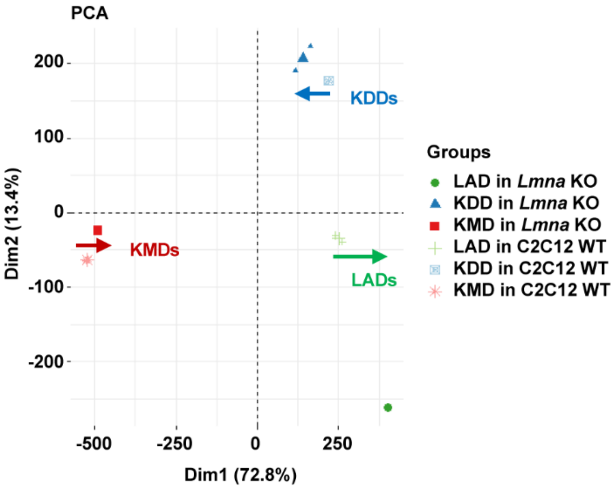

Supplementary Fig. S10. Alteration of histones and lamin-bound chromatin led to inhibition of adhesion-related genes.

PCA plot showing the similarity in structural domain features of LADs, KDDs and KMDs between C2C12 WT and *Lmna* cells.

Langtaosha (LTS) Preprint doi: https://doi.org/10.65215/ydw1ks77 This version posted November 19, 2025. The copyright holder for this preprint (which was not certified by peer review) is the author/funder. All Rights Reserved. No reuse allowed without permission.

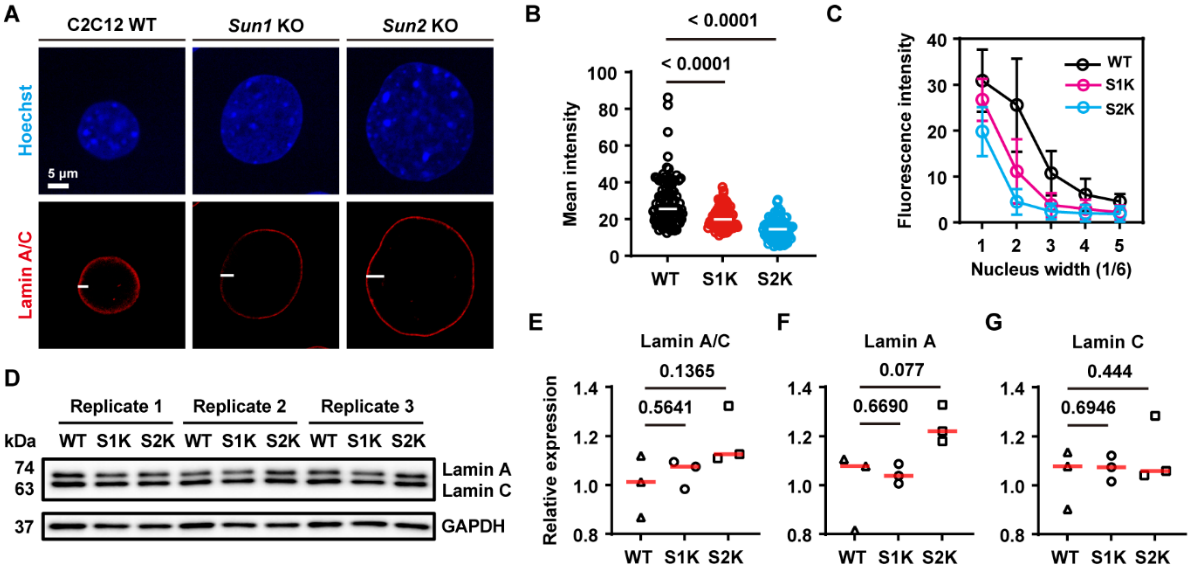

Supplementary Fig. S11. Perinuclear lamin A/C decreases upon *Sun1* or *Sun2* knockout.

(A) Immunofluorescence staining and imaging of nuclei and lamin A/C in C2C12 WT, *Sun1* KO, and *Sun2* KO cells (lamin A/C, n = 98, 97, 75 cells). Scale bar, 5 µm. The white line is one-sixth of the cell diameter.

(B) Quantification of lamin A/C mean intensity. Each dot represents a biological replicate, and white line segments indicate the mean values. One-way ANOVA.

(C) Line graph showing the distribution of lamin A/C fluorescence intensity across the nuclear periphery (white line segments). The x-axis divides the white line region into five equal regions. Data are presented as the mean with SD.

(D) WB analysis of lamin A/C protein levels in C2C12 WT, *Sun1* KO, and *Sun2* KO cells (three biological replicates per group).

(E-G) Quantification of lamin A/C (E), lamin A (F), lamin C (G) protein levels. Each dot represents a biological replicate, and red line segments indicate the mean values. One-way ANOVA.